Detection, localization and quantification of stiffness loss in a bridge using indirect drive-by measurements

Arturo González, Kun Feng* and Miguel Casero

School of Civil Engineering, University College Dublin, Dublin, Ireland

Correspondence: Kun Feng, School of Civil Engineering, University College Dublin, Dublin, Ireland. kun.feng@ucdconnect.ie.

ORCID

Arturo González, https://orcid.org/0000-0003-4942-1255

Kun Feng, https://orcid.org/0000-0003-1110-3681

Miguel Casero, https://orcid.org/0000-0001-9248-8231

Keywords

Bridge Structural Health Monitoring; Vehicle Bridge Interaction; Damage Detection.

Detection, localization and quantification of stiffness loss in a bridge using indirect drive-by measurements

Drive-by health monitoring uses the measurements gathered on a vehicle while traversing a bridge to assess its condition. To date, drive-by monitoring has been mostly proposed as a pre-screening tool to detect damage under favourable conditions of low vehicle speeds and low road roughness. A major shortcoming is the potential degradation of the road profile, which is often indistinguishable from bridge damage. In this paper, the influence of vehicle dynamics, speed, and road roughness is removed by applying cross-entropy optimization to the response of individual crossings of the vehicle at different speeds. The proposed model-based algorithm locates and quantifies damage while remaining unaffected by changes in the road profile. In addition to providing the distribution of bending stiffness in the underlying bridge, the algorithm isolates the bridge deflections accurately making the reconstruction of the actual road profile on the bridge possible. The latter can be a useful feature for ensuring traffic safety as well as preventing a major dynamic amplification of the bridge response. The algorithm is successfully tested for a quarter-car driving on a 15 m simply supported beam bridge model at highway speeds of 30 m/s over a class 'B' road with a roughness coefficient of 64×10^{-6} m^3/cycle.

Keywords: Drive-By; Bridge; Structural Health Monitoring; Damage Detection; Cross-Entropy; Transfer Function; Indirect Measurement; Road Profile; Stiffness Loss.

1. Introduction

The recent pandemic crisis has emphasized the need for the most efficient allocation of scarce resources. Within these needs, road infrastructure plays a fundamental role in

fulfilling the demands of our society. In particular, bridge structures have to be monitored to ensure that the network remains operational and safe at all times. Additionally, it would be desirable to keep bridges near the end of their design life operational when displaying good condition to minimize the strain on governmental budgets and environmental costs. Nevertheless, the recent collapses of the Malahide viaduct in Ireland (Railway Accident Investigation Unit [RAIU], 2010), the Polcevera viaduct in Italy (Domaneschi et al., 2020), and the Mirepoix-sur-Tarn bridge in France (Engineering News-Record [ENR], 2019), underline the emergency for implementing more efficient and practical Structural Health Monitoring (SHM) systems.

Visual inspections are still the most popular approach to assessing the health of bridges, but they are prone to a high degree of subjectivity and are usually separated by one or more years. Ideally, a bridge stock would be monitored on a continuous basis using measurements of the response to operational loads through sensors directly attached to the bridges. This approach, known as direct SHM, dominates the traditional bridge condition assessment due to its real-time diagnostic capability and high accuracy (Soman et al., 2018), but a large sensor network, power supplies and a data acquisition system are required to be mounted on each selected bridge to gather the required input. Necessarily, such a management strategy can only be implemented on a small scale due to prohibitive installation and maintenance costs.

Unlike direct SHM, an indirect approach pioneered by Yang et al. (2004) relies on only one or a few sensors attached to a vehicle rather than to the bridge, the so-called drive-by SHM. Considering its efficiency and low-cost potential, the drive-by method has been validated via theoretical (McGetrick et al., 2009; Yang et al., 2004), laboratory (Kim et al., 2017; Liu et al., 2020), and field (Lin & Yang, 2005; Siringoringo & Fujino, 2012) tests. As pointed out by Yang and Lin (2005), drive-by measurements contain vehicle,

bridge, and road components. Moreover, the frequency spectrum is usually dominated by the vehicle components, and the identification of the bridge components is problematic. Consequently, how to isolate the bridge components buried within the drive-by measurements is one of the key questions to be addressed in research on drive-by SHM. The separation of bridge components from vehicle and road components becomes more challenging as vehicle speeds and road roughness increase.

Rytter (1993) proposes four levels of structural damage identification: I - able to detect the presence of damage, II - able to detect and locate the damage, III - able to detect, locate and quantify the damage, and IV - able to detect, locate and quantify the damage and to estimate the remaining life of the structure. In general, model-based methods (Alves & Cury, 2021; Chen et al., 2018; He et al., 2019) provide more detailed and reliable condition information on the bridge structure than data-driven or non-model-based methods (He et al., 2018; Malekzadeh et al., 2014; Yin et al., 2017). The latter could be used to identify or locate the damage, but they are usually unable to quantify it due to the lack of detailed information about the geometry and mechanical properties of the bridge. Therefore, non-model-based methods typically require a reference baseline when the structure is assumed to be healthy. On the one hand, research on direct SHM is very extensive, and it can involve both data-driven and model-based algorithms, as well as all four damage identification levels. On the other hand, research on indirect approaches is data-driven normally and confined to levels I and II.

In the absence of a bridge, the Transfer Function (TF) of a vehicle has been employed before to classify a road profile using drive-by measurements in the frequency domain (González et al., 2008), in contrast to other techniques based in the time domain (Harris et al., 2010; Keenahan et al., 2019). Cross-entropy optimization has also been shown as a valid method for updating a Finite Element Model (FEM) based on

measurements of the response directly taken from the structure (Dowling et al., 2012). Both techniques are brought together here to propose a novel model-based indirect approach capable of detecting, locating and quantifying bridge damage. The ability of the algorithm to assess damage is demonstrated using the acceleration response of a quarter-car (QC) traversing a bridge beam model. Section 2 provides background information on the subject before Section 4 dives into the details of the methodology. Section 3 describes the properties and coupled equations of the vehicle-bridge interaction (VBI) model, the road profile and the damage model used to simulate the stiffness loss in the structure. Sections 5, 6 and 7 evaluate and compare results for scenarios with different locations and severities of a crack and two road classes. Section 8 analyses the sensitivity of the algorithm to bridge damping, vehicle speed and changes in the transverse location of the vehicle. Finally, Section 9 gives conclusions and suggestions for further research.

2. Background

Several data-driven level II drive-by techniques based on a quasi-static application of the load, i.e., moving at very low speeds ≤ 1 m/s, are available in the literature. Instantaneous frequencies are the basis of some of these techniques (Hester & González, 2017), but the scope of time-frequency signal processing tools is limited to good road conditions and measurements of relatively long duration, i.e., low speeds and/or long bridge spans, to prevent contamination due to edge effects. In practice, the use of low speeds is likely to involve road closures or disruptions to the traffic flow. Even further, the worsening in the road condition is reported as a major impediment to reaching just level I (Hester & González, 2015, 2017).

In order to deal with typical traffic speeds and rough road profiles, OBrien and Keenahan (2015) propose a level I damage indicator based on the time-shifted difference

of the apparent profiles between the front and rear axles. The apparent profile refers to the displacement that would be measured from a straight line on the vehicle to the road surface over the bridge. By computing the differences between the apparent profile measured from each axle, which contains both the irregularities of the road profile and the bridge displacements, the impact of the road is reduced and the changes in bridge deflections due to damage are amplified. The algorithm is tested theoretically by simulating the crossing of a two-axle half-car model moving at 20 m/s over a 20 m simply supported beam with an ISO 8608 class 'A' road profile (International Organization for Standardization [ISO], 2016). Some drawbacks are the need for costly traffic speed deflectometers to capture the displacements of the vehicle, the strict requirement for equal mechanical properties in the axles, and the sensitivity of results to noise due to the small values resulting from the subtraction of the apparent profiles. Elhattab et al. (2016) use a QC model moving at 25 m/s over 10, 20 and 30 m simply supported bridges with an 'A' roughness class to simulate the drive-by acceleration, which is then used to calculate the apparent profile. Numerical results confirm that the difference in the apparent profiles between a healthy and a damaged beam is sensitive to local damage on a bridge, however, no changes in the road profile are considered. Furthermore, Quirke et al. (2017) use train-based inertial measurements to determine the apparent profile, when the train is modelled travelling over a 16.08 m simply supported beam at 41.6 m/s. In this work, changes in the area between the apparent profile and the zero elevation are proposed as a level I damage detection algorithm. Again, the authors rely on the assumption that the changes in track irregularities between two different inspection times are negligible.

The latest publications on drive-by SHM place focus on the response of the contact point between the vehicle and the bridge (Corbally & Malekjafarian, 2021; Nayek & Narasimhan, 2020; Zhan et al., 2020; Zhan et al., 2021). Yang et al. (2018) derive the

theoretical equation characterizing the displacement of the point under a moving axle. The VBI model is a lumped mass supported by a spring moving over a simply supported beam at a constant speed. The theoretical results confirm that the dynamic response under the moving axle is free of vehicle components and contains more detailed bridge information than those responses measured on the vehicle body. Having removed or reduced the vehicle components, the road components remain the last obstacle to be overcome. There are several techniques in the literature for this purpose, i.e., subtraction-based algorithms in the time domain (Keenahan & OBrien, 2018; Tan et al., 2017), subtraction-based algorithms in the frequency domain (Kim et al., 2017; Yang et al., 2012), and signal processing techniques, like blind source separation (Li et al., 2019). However, the success of these algorithms usually requires that the vehicle has axles with identical properties for subtraction purposes, and that the frequency range of the bridge is known prior to the application of the filtering and separation algorithm. Therefore, these algorithms capture changes in the response that could denote the presence of damage, but the damage is rarely located or quantified accurately, i.e., in terms of stiffness loss at a specific bridge section, and most frequently, they remain at damage detection level I or II.

This paper proposes a level III damage detection algorithm applicable to drive-by measurements collected at high speeds over rough road profiles that can change over time, as follows:

(1) Interaction forces between vehicle and bridge, and displacements of the contact point, are obtained for a speed v_1 via one of the following two options:

   a. Vertical acceleration data from accelerometers mounted on the axles of a vehicle. Accelerations are relatively easy to measure in motion compared to other responses such as displacements. The displacement of the axle is

obtained via integration of the measured acceleration. By utilizing the TF, the Fast Fourier Transform (FFT) and its inverse FFT, the vertical displacement of the contact point can be extracted from the vertical acceleration of the axle in the time domain. The time history of contact forces is then obtained from the relative displacements between the contact point and the axle based on known tyre properties concerning stiffness and damping.

b. Force and/or displacement data (i.e., using laser sensors) from a specialized instrumented vehicle (Fernando et al., 2007; Liu et al., 2023) or traffic speed deflectometer (Chai et al., 2016; Keenahan & OBrien, 2018). This option, although more costly, avoids errors associated with the integration process required by the alternative option (1)-a.

(2) The time-varying contact forces are applied to different sections of a FEM of the bridge to obtain the bridge deflection as the vehicle moves along. For this purpose, a stiffness profile needs to be assumed.

(3) The road profile is obtained by subtracting the displacement of the bridge in step (2) from the displacement of the contact point in step (1).

(4) Steps (1) to (3) are repeated to obtain the deflections of the bridge and the road profile for a different speed v_2. The same stiffness profile as in step (2) must be employed. The algorithm relies on the fact that for the true stiffness profile, the same road profile should be obtained regardless of the vehicle speed. Thus, the stiffness profile is updated in successive iterations (loop covering steps (2) to (4)) using a cross-entropy optimization procedure that minimizes an objective function defined by the difference between the road profiles predicted at both speeds.

3. Numerical models

3.1. Definition of vehicle and bridge models

Figure 1 shows the VBI model, composed of a QC and a simply supported FEM of a beam, used in the simulations.

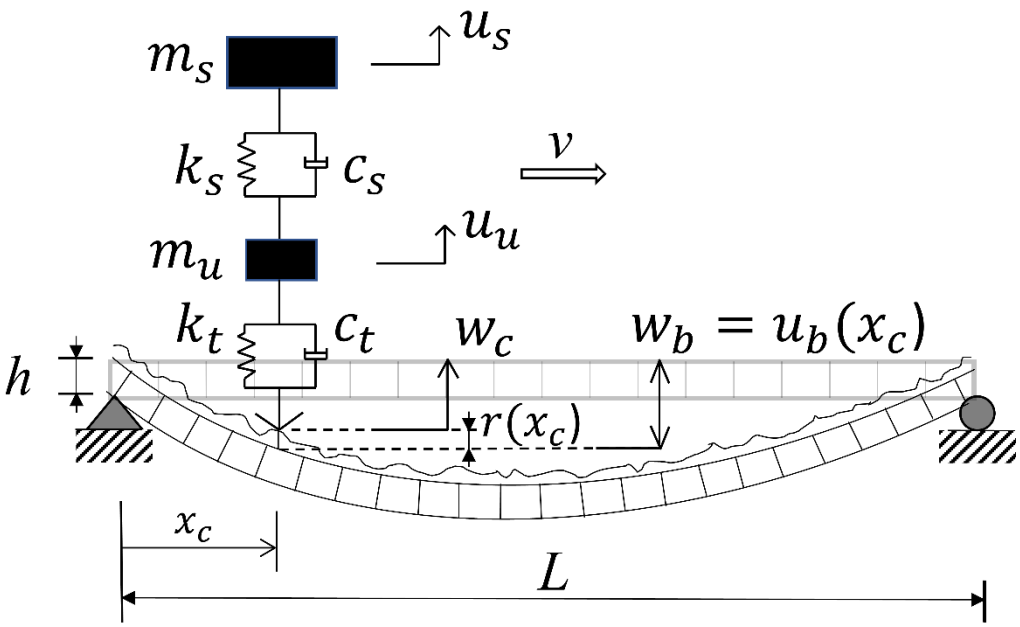

Figure 1. QC-based VBI model

The mass, damping and stiffness matrices of the QC model can be expressed as:

$$[M_v] = \begin{bmatrix} m_s & 0 \\ 0 & m_u \end{bmatrix};\ [K_v] = \begin{bmatrix} k_s & -k_s \\ -k_s & k_s + k_t \end{bmatrix};\ [C_v] = \begin{bmatrix} c_s & -c_s \\ -c_s & c_s + c_t \end{bmatrix} \quad (1)$$

where m_s and m_u are the sprung and unsprung masses, k_s and k_t represent the suspension and tyre stiffness, and c_s and c_t correspond to the suspension and tyre damping, respectively. Table 1 gives the values of the parameters of the vehicle based on Green and Cebon (1994), where the 1st and 2nd frequencies of the QC vehicle are 3.18 and 23.93 Hz, respectively.

Table 1. Properties of QC model

Parameter	Value	Unit
Gross vehicle weight, P	392	kN
Sprung mass, m_s	36×10^3	kg
Unsprung mass, m_u	4×10^3	kg
Suspension stiffness, k_s	18×10^3	kN/m
Tyre stiffness, k_t	72×10^3	kN/m
Suspension damping, c_s	144	kN s/m
Tyre damping, c_t	144	kN s/m

A span (L = 15 m) to depth (h = 0.75 m) ratio of 20, typical of short-span bridges, and simply supported boundary conditions, are adopted for the bridge. The 2nd moment of area (I) equals 0.5273 m^4, and common concrete properties are chosen for the modulus of elasticity (E = 35 GPa) and mass per unit length (m = 28125 kg/m). As a result, the first three bridge frequencies are 5.66, 22.62 and 50.90 Hz. Damping is typically low in bridge structures, and it is neglected here unless otherwise specified. The FEM of the bridge consists of discretizing the span into 150 beam elements. Each beam element has two Degrees of Freedom (DoFs) per end node, i.e., vertical translation and rotation. The bridge mass $[M_b]$ and stiffness matrices $[K_b]$ are created by assembling the 150 beam elementary matrices and have dimensions of 302 × 302.

3.2. Equations of motion for coupled VBI system

A comprehensive review of the implementation of the VBI procedure is available in the literature (González, 2010). The approach adopted in this paper defines the coupled equation of motion as:

$$[M_g]\{\ddot{u}_g\} + [C_g]\{\dot{u}_g\} + [K_g]\{u_g\} = \{F_g\} \tag{2}$$

where $[M_g]$, $[C_g]$ and $[K_g]$ correspond to the global mass, damping and stiffness matrices, respectively. The vectors $\{F_g\}$ and $\{u_g\} = \begin{Bmatrix} u_v \\ u_b \end{Bmatrix}$ contain the global forces and the unknown displacements, whereas $\{u_v\} = \begin{Bmatrix} u_s \\ u_u \end{Bmatrix}$ and $\{u_b\}$ denote the displacements of the vehicle and the bridge separately. The superscripts $\{\dot{u}_g\}$ and $\{\ddot{u}_g\}$ in Equation (2) indicate the 1st and 2nd derivatives with respect to time of the global displacement $\{u_g\}$, respectively. The global mass $[M_g]$, damping $[C_g]$ and stiffness $[K_g]$ matrices are determined by:

$$[M_g] = \begin{bmatrix} M_v & 0 \\ 0 & M_b \end{bmatrix}; [C_g] = \begin{bmatrix} C_v & C_{vb} \\ C_{bv} & C_b + C_{bb} \end{bmatrix}; [K_g] = \begin{bmatrix} K_v & K_{vb} \\ K_{bv} & K_b + K_{bb} \end{bmatrix} \quad (3)$$

In Equation (3), C_{bv}, C_{bb}, C_{vb}, K_{bv}, K_{bb} and K_{vb} are time-varying matrices that depend on the location of the vehicle and can be computed according to:

$$C_{bv} = \{N_b\}\{0, c_t\}; C_{vb} = C_{bv}^T; C_{bb} = \{N_b\}\{\{N_b\}c_t\}^T \quad (4)$$

$$K_{bv} = \{N_b\}\{0, k_t\}; K_{vb} = K_{bv}^T; K_{bb} = \{N_b\}\{\{N_b\}k_t\}^T \quad (5)$$

where the superscript T denotes the transpose of a matrix and $\{N_b\}$ is the location vector at a given instant in time. The vector $\{N_b\}$ has dimensions 302 × 1, and the components take a value of zero for those DoFs of the bridge not corresponding to the element where the vehicle is located at a given moment in time. For the four DoFs of the element i where the vehicle is located, the components of the vector $\{N_b\}$ are given by the following shape functions:

$$\{N_b\} = \begin{Bmatrix} \cdots \\ 1 - 3\left(\frac{x_c - (i-1)L_e}{L_e}\right)^2 + 2\left(\frac{x_c - (i-1)L_e}{L_e}\right)^3 \\ (x_c - (i-1)L_e) - \frac{2(x_c - (i-1)L_e)^2}{L_e} + \frac{(x_c - (i-1)L_e)^3}{L_e^2} \\ 3\left(\frac{x_c - (i-1)L_e}{L_e}\right)^2 - 2\left(\frac{x_c - (i-1)L_e}{L_e}\right)^3 \\ -\frac{(x_c - (i-1)L_e)^2}{L_e} + \frac{(x_c - (i-1)L_e)^3}{L_e^2} \\ \cdots \end{Bmatrix} \quad (6)$$

where i = 1, 2, …, 150 refers to the underlying beam element, L_e to its length (i.e., L_e = 0.1 m), and the variable x_c corresponds to the location of the axle measured from the left support of the beam (i.e., $0 \leq x_c \leq 15$ m). The 1st and 3rd shape functions in Equation (6) are related to the vertical translation, and the 2nd and 4th shape functions correspond to the rotations of the left and right end nodes, respectively. Equation (7) defines the global force vector, $\{F_g\}$.

$$\{F_g\} = \begin{Bmatrix} 0 \\ k_t r + c_t \dot{r} \\ -\{N_b\}\left(P - (k_t r + c_t \dot{r})\right) \end{Bmatrix} \quad (7)$$

where r represents the height of the road profile under the contact point and $\dot{r}$ corresponds to its 1st derivative. Finally, the coupled equations of motion are coded with MATLAB R2021b and integrated using the Newmark-beta method with γ = 0.5 and β = 0.25 to derive the vertical acceleration of the axle, $\{\ddot{u}_u\}$. The latter will serve as input to the drive-by algorithm tested in further sections.

3.3. Road profile and bridge damage model

The importance of the road profile on the response of both the vehicle and the bridge is well documented regarding the dynamic amplification of the interaction forces caused by a rough road (Camara et al., 2017). The road profile is considered as a time series of

measurements of the vertical displacement of the road surface over a distance. Here, it is assumed that the statistical properties of the road surface do not change over time and that the road surface can be represented as a random process with the vertical displacement at any given point being a random variable. The height of the road irregularities is then a zero-mean stationary Gaussian random process (Cebon & Newland, 1983), which is theoretically generated through an inverse FFT of its Power Spectral Density (PSD) function (Agostinacchio et al., 2014). The latter is adopted from ISO 8608 (2016), which relies on the PSD of a reference spatial frequency, $G_d(n_0)$, to categorize the quality of the road from class 'A' (the best rating) to 'H' (the worst rating). For instance, $G_d(n_0)$ varies from 0 to 32×10^{-6} m^3/cycle for road class 'A', and from 32×10^{-6} to 128×10^{-6} m^3/cycle for road class 'B'.

In this paper, the road profile is made of 10501 sinusoidal waves with equally spaced frequencies between 0.0014 cycle/m and 8.2344 cycle/m, amplitudes depending on the frequency and PSD, and phase angles uniformly distributed between 0 and 2π. The length of the simulated road profile allows for a 60 m approach road before the 15 m bridge. The implementation of an approach road prior to the bridge is necessary for the vehicle model to reach dynamic equilibrium and to establish realistic initial conditions for the DoFs of the vehicle when entering the bridge. Although the road profile may have characteristics that cannot be modelled as a zero-mean Gaussian stationary process, the definition of the profile in the spatial domain would remain unaltered when crossed by the vehicle at a different speed. Therefore, the profile could be subjected to the same optimization procedure that will be proposed further on.

Regarding the damage model, the stiffness reduction proposed by Sinha et al. (2002) is used to simulate the effect of a crack in the bridge. The damage severity is expressed by the ratio $\lambda = 100 \times h_d/h$, where h_d is the crack depth and h is the bridge

depth. In Sinha's model, stiffness increases linearly from a minimum at the crack location to a maximum (i.e., healthy condition) at a distance of $1.5h$ from both sides of the crack (Garrido et al., 2020).

4. Level III drive-by algorithm

Figure 2 shows a flow chart of the proposed algorithm. It is necessary to obtain the response of the vehicle for two different speeds to separate the effect of the road profile from the displacement of the bridge. For convenience, speeds of 15 m/s and twice faster, 30 m/s, are chosen, to facilitate a comparison of road irregularities at the same locations without the need for interpolation. Then, the distribution of bending stiffness throughout the bridge is calculated by minimizing the differences in the road profile estimated at each speed. The bending stiffness is defined as the multiplication of the modulus of elasticity (E) by the 2nd moment of area of the cross-section (I).

4.1. Step (1) – Estimation of displacements and forces at the contact point

It is worth pointing out that there are specialized vehicles able to measure the vertical displacement of the contact point via lasers directly (Chai et al., 2016), as well as the applied forces, in which case it is possible to jump straight into step (2) of the algorithm. Such vehicles would overcome many of the challenges posed by deriving the contact point displacement from a different measured response. However, it is acknowledged that these vehicles, although commercially available, are rare and expensive. An alternative low-cost method based on accelerations easily measured via accelerometers mounted on the axle and the subsequent application of the TF of the vehicle, FFT and its inverse transform, can also be employed to obtain displacements and forces of the contact point in a more accessible manner.

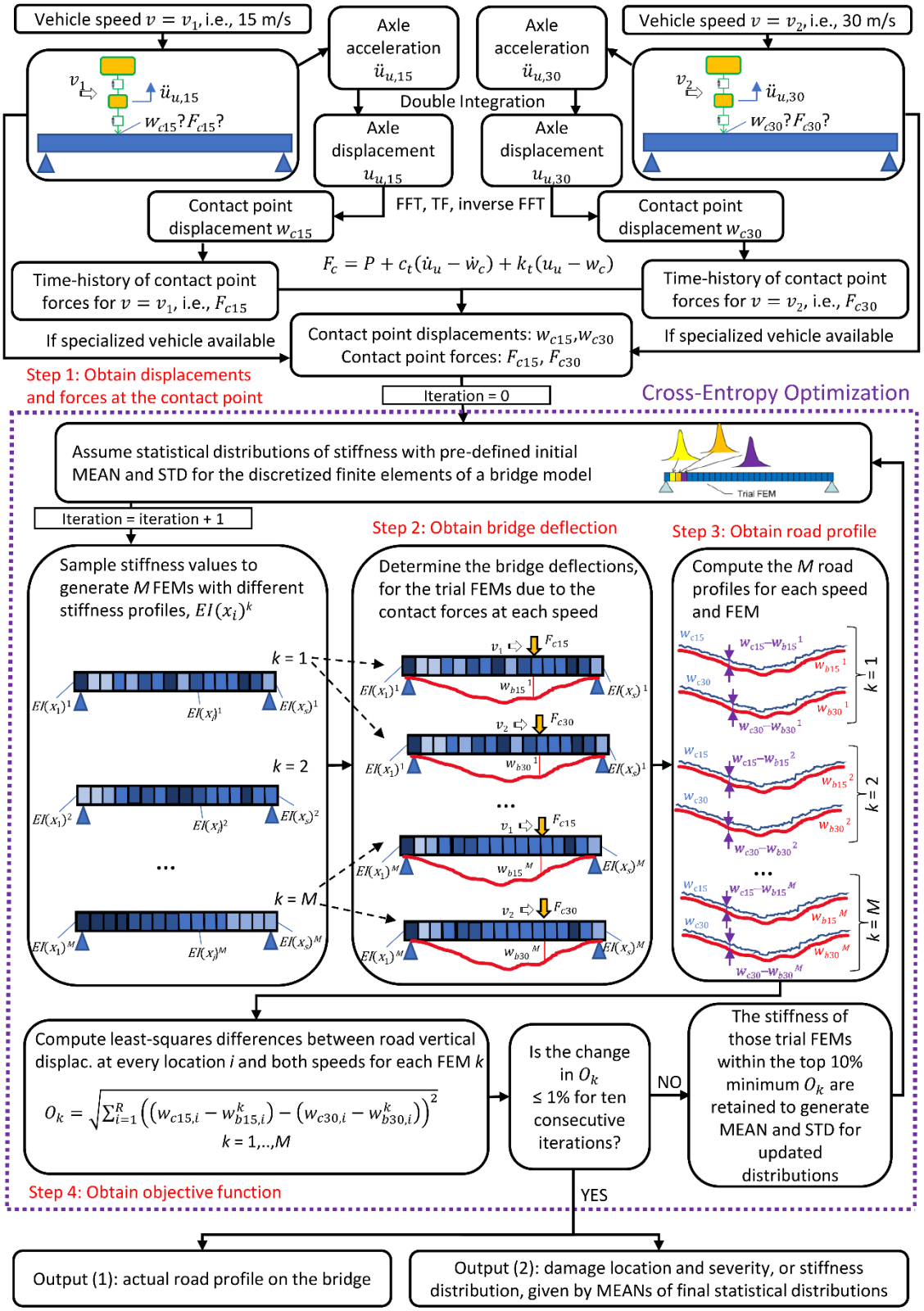

Figure 2. Flow chart of drive-by algorithm to locate and quantify damage

In the absence of field measurements, accelerations are simulated for the unsprung mass of a QC moving at a constant speed of 15 m/s over a road stretch defined following Section 3.3 for a roughness class 'A' based on a geometric spatial mean of $G_d(n_0)$ = 0.1 × 10^{-6} m^3/cycle. The starting point of the road profile employed in the simulations is assumed to have zero height. The displacement of the unsprung mass, u_u, can be calculated by applying the cumulative trapezoidal numerical integration twice to the acceleration, $\ddot{u}_u$ (Yeh & Kwan, 1978). Moreover, if the FFT is applied to the time-history of displacements, the real and imaginary parts of the response are obtained in the frequency domain. The TF is then used to reconstruct the displacement of the contact point from the displacement of the unsprung mass in the frequency domain. The TF can be established experimentally by measuring the axle acceleration due to a road with a known profile. For a simple QC model, the theoretical TF is attainable from the differential equations of motion given by (Karnopp, 2009; Barbosa, 2011):

$$m_s\ddot{u}_s + c_s(\dot{u}_s - \dot{u}_u) + k_s(u_s - u_u) = 0 \tag{8}$$

$$m_u\ddot{u}_u + c_t(\dot{u}_u - \dot{w}_c) + k_t(u_u - w_c) - c_s(\dot{u}_s - \dot{u}_u) - k_s(u_s - u_u) = 0 \tag{9}$$

where u_s, u_u, w_c represent the displacement of the sprung mass, the unsprung mass, and the contact point between the axle and bridge surface, respectively (Figure 1). The $\dot{u}_s$, $\dot{u}_u$, $\dot{w}_c$ and $\ddot{u}_s$, $\ddot{u}_u$, corresponding to the 1st and 2nd derivatives refer to the related velocities and accelerations. According to the theory of the Fourier transform, Equations (8) and (9) can be rearranged as:

$$m_s(j\omega)^2U_s + c_s(j\omega)(U_s - U_u) + k_s(U_s - U_u) = 0 \tag{10}$$

$$m_u(j\omega)^2U_u + c_t(j\omega)(U_u - W_c) + k_t(U_u - W_c) - c_s(j\omega)(U_s - U_u) - k_s(U_s - U_u) = 0 \tag{11}$$

Based on the above two equations, Equation (12) gives the TF of the unsprung mass, which can be obtained as the ratio between the Fourier transform of the axle response and the Fourier transform of the contact point response:

$$TF = \frac{U_u(j\omega)}{W_c(j\omega)} = \frac{(j\omega c_t + k_t)(m_s(j\omega)^2 + j\omega c_s + k_s)}{\left(m_s(j\omega)^2 + j\omega c_s + k_s\right)\left(m_u(j\omega)^2 + j\omega c_t + k_t\right) + m_s(j\omega)^2(j\omega c_s + k_s)} \quad (12)$$

where $U_u(j\omega)$ and $W_c(j\omega)$ denote the Fourier transforms of u_u and w_c, respectively; j is the imaginary unit and ω is the circular frequency. Figure 3 depicts the real and imaginary components of the TF of the unsprung mass of a QC.

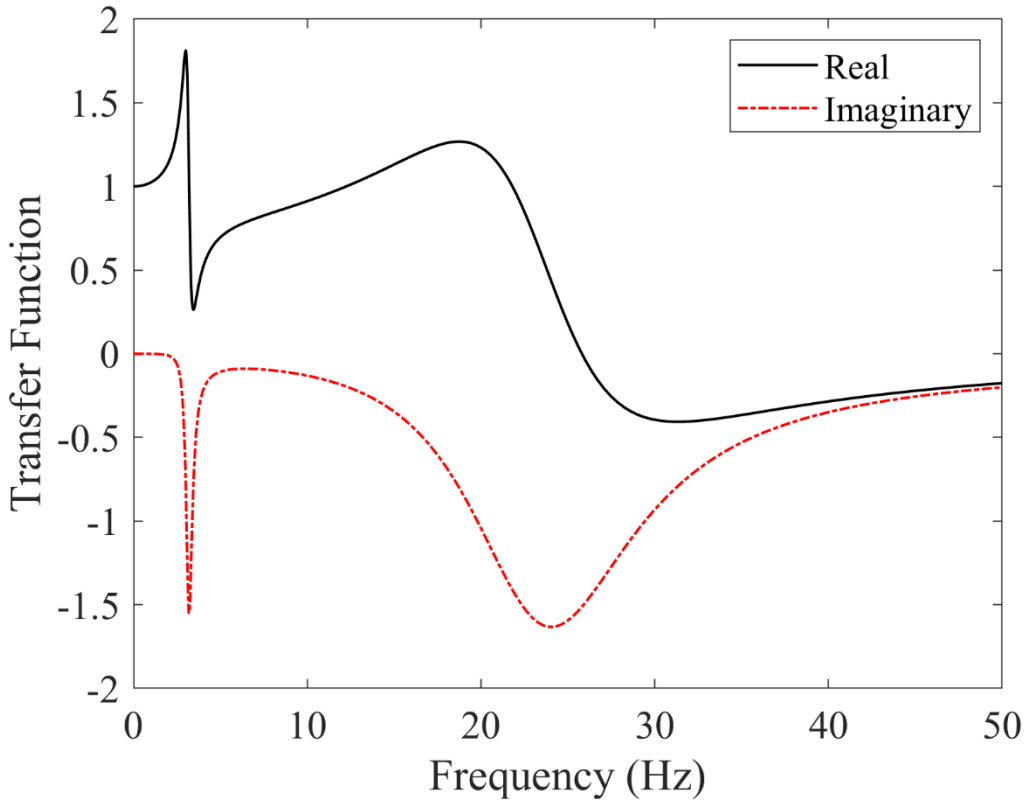

Figure 3. Real and imaginary components of the TF between the displacements of the unsprung mass and the contact point

After dividing the real and imaginary parts of the frequency response of the unsprung mass by the relevant TF in Figure 3, the displacement of the contact point is obtained in the frequency domain. Figure 4 shows the displacement of the contact point in the time domain after applying the inverse FFT to the response in the frequency domain. Figure 4(a) compares the true and the estimated displacements of the contact point, whereas Figure 4(b) shows the estimated displacement of the unsprung mass (via integration) and the estimated displacement of the contact point when the vehicle is located on the bridge.

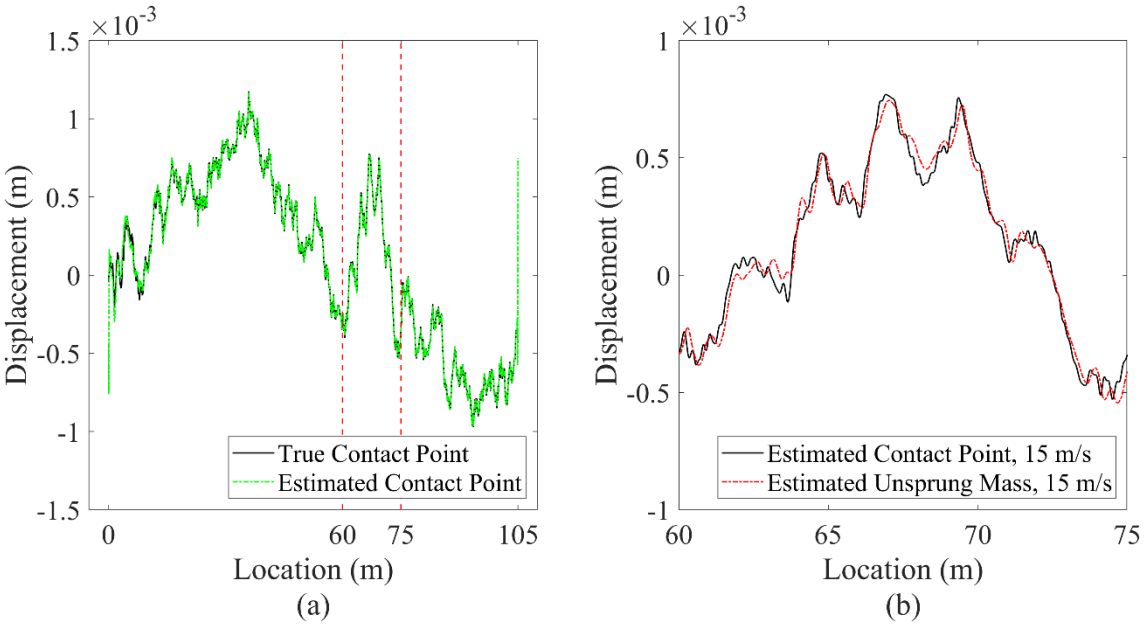

Figure 4. Comparison between displacements of (a) true and estimated contact point, (b) estimated contact point and estimated unsprung mass on the bridge

Once w_c is found, Equation (13) can be employed to derive the corresponding time series of contact forces from the relative responses between the contact point and the axle.

$$F_c = P + c_t(\dot{u}_u - \dot{w}_c) + k_t(u_u - w_c) \tag{13}$$

where F_c represents the total contact force, made of a static component, P, and a dynamic component depending on the variables, u_u, w_c, $\dot{u}_u$ and $\dot{w}_c$. The last two variables are computed via differentiation of the displacement, u_u or w_c, versus time series. Equation (13) requires the tyre properties of the vehicle to be known. The contact forces, F_c, must be obtained for at least two runs of the vehicle over the bridge at different speeds.

It is worth mentioning that two integration constants arise from the integration process that extracts u_u from $\ddot{u}_u$: the initial displacement, $(u_u)_0$, and the initial velocity, $(\dot{u}_u)_0$. The latter is responsible for the linear drift that can be observed in displacements as a result of integrating accelerations that rely on inaccurate initial conditions. To correct the linear drift, the initial velocity, $(\dot{u}_u)_0$, can be estimated through minimisation of the sum of the time-varying dynamic components of the contact force (2nd and 3rd terms of Equation (13)) acting on the road prior to the bridge, provided that the distance is sufficiently long. This approach is based on the nature of the dynamic component that tends to compensate for oscillations of the total force above and below the static component. Once an estimation of the initial velocity becomes available, the initial displacement, $(u_u)_0$, can be obtained by minimizing the differences in the height of the road irregularities estimated at each speed before the vehicle enters the bridge (i.e., $w_c = r$).

4.2. Steps (2) to (4) – Estimation of bridge deflection, road profile and objective function

The contact forces obtained in step (1) are applied to a FEM of the bridge to calculate the time-varying displacements of the bridge underneath the contact point. This calculation requires knowing the stiffness profile of the bridge, which will have to be initially assumed based on the dimensions of the cross-section and typical material properties. The first estimation of the variation in stiffness throughout the bridge will be improved in

successive iterations through a cross-entropy optimization iterative procedure. In every iteration, M trial FEMs with different stiffness profiles are generated. For each trial FEM, the equation of motion of the bridge (Equation (14)) is solved for the time history of contact forces obtained in step (1), and the time series of the bridge deflection under the contact point, w_b, is found via the location vector as per Equation (15). This is step (2) of the flow chart in Figure 2.

$$[M_b]\{\ddot{u}_b\} + [C_b]\{\dot{u}_b\} + [K_b]\{u_b\} = \{F_c\} \tag{14}$$

$$w_b = \{N_b\}^T\{u_b\} \tag{15}$$

Step (3) consists of obtaining the differences between the displacement of the contact point, w_c, and the bridge deflection, w_b. The reason is twofold:

- This difference should be equal to the road profile, r, if the stiffness distribution of the trial FEM was identical to that of the real bridge.
- The road profile, r, is independent of the vehicle speed.

Based on the differences $(w_c - w_b)$ for two speed scenarios, i.e., 15 and 30 m/s, the following objective function is defined (step (4)) for a FEM labelled k:

$$O_k = \sqrt{\sum_{i=1}^{R}((w_{c15,i} - w_{b15,i}^k) - (w_{c30,i} - w_{b30,i}^k))^2} \quad , \quad k = 1, 2, 3, \dots, M \tag{16}$$

where $w_{c15,i}$ and $w_{c30,i}$ are the displacements of the contact point at 15 and 30 m/s respectively, i represents a load location along the bridge, and R the total number of equally spaced locations being compared; $w_{b15,i}^k$ and $w_{b30,i}^k$ are the bridge deflections at each load location i and trial FEM number k.

Steps (2) to (4) of the proposed algorithm are framed within the cross-entropy procedure as described next:

i. Initial normal distributions characterized by mean and standard deviation are assumed for the unknowns under analysis. Two unknowns (location and severity of a Sinha's damage type) are considered in Section 5, whereas *s* unknowns representing the stiffness, *EI*, of *s* beam segments are evaluated in Sections 6, 7 and 8.

ii. *M* FEMs (trial beams) are randomly generated by sampling values from the statistical distributions assumed for each unknown. M = 500 is used in this paper.

iii. For each trial beam *k*, Equations (14) and (15) are solved to obtain the bridge displacements at 15 and 30 m/s, w_{b15}^{k} and w_{b30}^{k}. Subsequently, the differences between bridge deflections and contact point displacements are computed, $(w_{c15} - w_{b15}^{k})$ and $(w_{c30} - w_{b30}^{k})$. These are steps (2) and (3) in the flow chart from Figure 2.

iv. The objective function O_k is calculated according to Equation (16) for each trial beam. The objective function will tend to zero as the road profiles predicted at 15 and 30 m/s get closer, which means that the trial FEM experiences a similar damage event to the real bridge. The calculation of the objective function represents step (4) of the overall algorithm as per Figure 2.

v. The *M* trial beams are ranked according to the value of O_k and those within the top 10%, i.e., corresponding to the minimum values of the objective function, are retained to update the mean and standard deviation of the normal distributions to be sampled for each elementary beam in the next iteration.

vi. Points (ii) to (v) of the cross-entropy procedure are repeated until convergence occurs. Here, the iterative process will be stopped when the change in the objective function is found to remain below 1% for ten consecutive iterations.

Once this stopping criterion is met, the value of the mean of the normal distribution in the last iteration is proposed as the solution.

5. Prediction of a damage scenario known to follow Sinha's model

This section makes the simplifying assumption that the damage type (Sinha's model) and the healthy condition of the bridge (EI) are known. Therefore, the optimization procedure only has two unknowns: the location and depth of the crack. Once these two variables are established, the entire stiffness profile can be defined based on Sinha's theory. Sinha's crack to be sought is located at 5 m from the left support with λ = 20%. The same class 'A' road profile as in Section 4.1 and speeds of 15 and 30 m/s are adopted here.

Figures 5(a), 5(b) and 5(c) present the displacements of the contact point (w_c), the contact forces (F_c) applied to the bridge and the bridge deflections underneath the moving load (w_b), respectively, at the two speeds. Figure 5(a) contains bridge deflections in addition to road irregularities. Therefore, the subtraction of Figures 5(a) and 5(c) should lead to the road profile ($r(x_c)$) if the FEM was experiencing a similar damage to the tested bridge, i.e., a crack located at 5 m with λ = 20%. Similarly, there should be a match between the road predictions at 15 and 30 m/s since the road profile is independent of the moving speed. If there was a mismatch in the road profile predicted at both speeds, it is understood that the FEM will have not located and/or quantified the damage properly, except for noise and modelling errors.

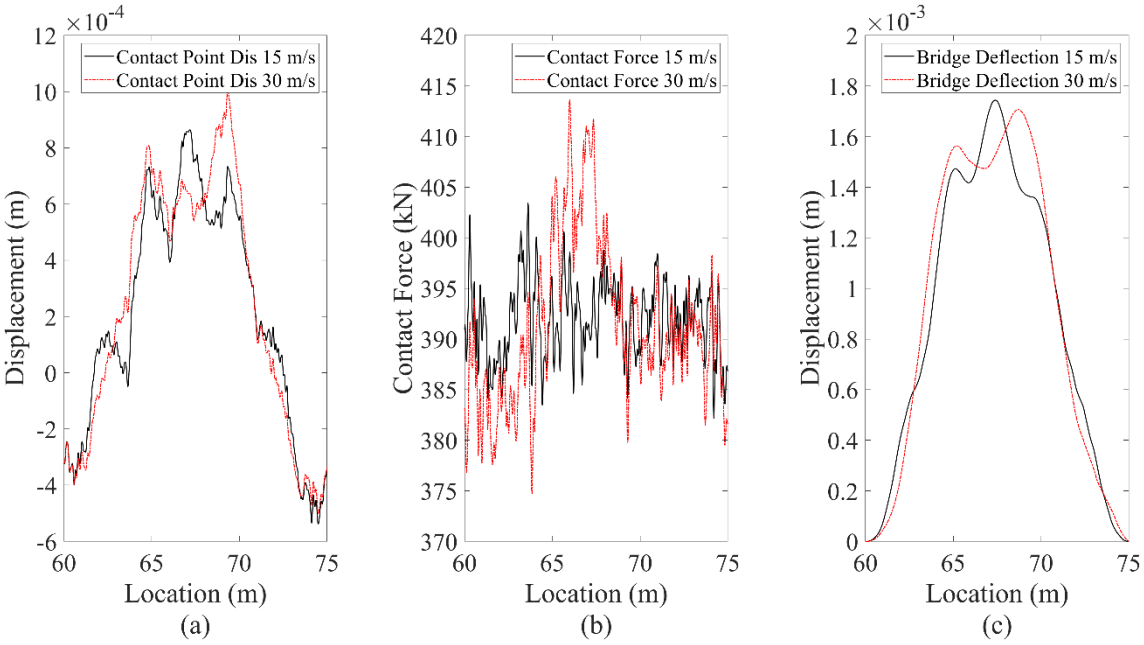

Figure 5. Results obtained at 15 and 30 m/s versus location of QC for: (a) displacement of the contact point, (b) contact forces, and (c) bridge deflections

The contact forces in Figure 5(b) are input into the cross-entropy optimization procedure. The location and severity of damage are the two random variables to be found. Firstly, the initial mean and standard deviation of the normal distribution for the location are adopted to be 7.5 m and 2.5 m respectively, while the initial mean and standard deviation of the severity are set to be 0.375 m and 0.125 m respectively. These values lead to a 99.74% probability that the random sampling will produce values within [0 - 15 m] of the bridge with a crack depth within the range [0 - 0.75 m]. There is always a small chance of sampling damage scenarios outside the physically feasible range that would need to be disregarded and replaced by realistic FEM scenarios. Then, the cross-entropy procedure explained in Section 4.2 is implemented. Figure 6 indicates how the estimated location and severity (λ) evolve in the first 20 iterations. The filled square and the error bar cap represent the mean value and standard deviation of the statistical distribution at each iteration. After ten iterations, the cross-entropy procedure is not making further progress and the suggested location and severity are very close to the exact solution, i.e.,

the predicted mean values at the tenth iteration for damage location and severity are 4.99 m with λ = 19.73%, corresponding to errors of 0.20% and 0.27%, respectively.

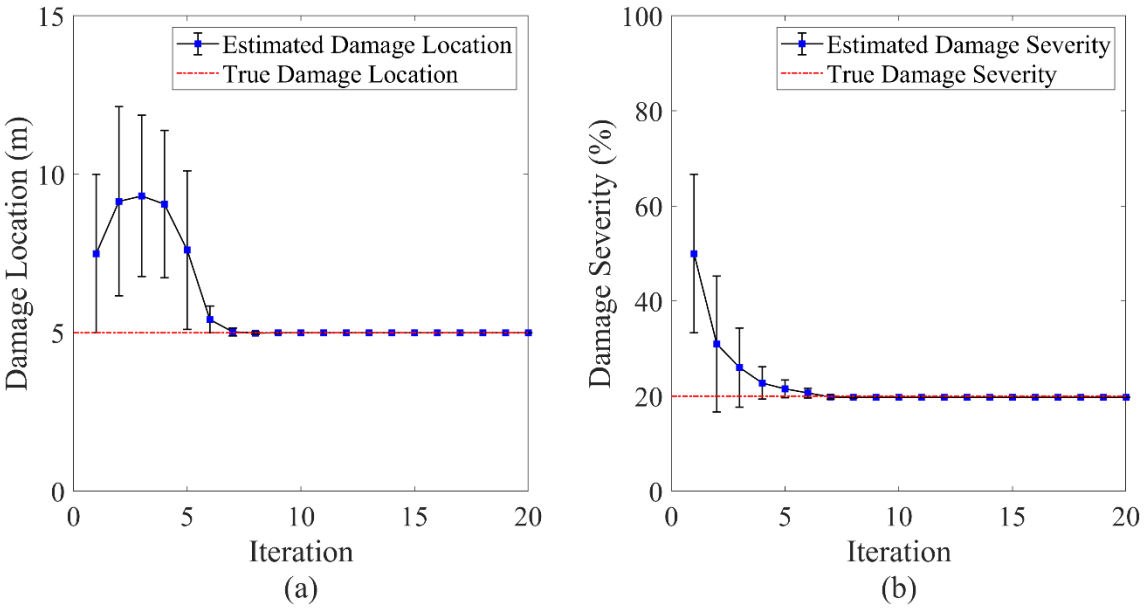

Figure 6. Prediction of damage at each iteration: (a) location, (b) severity

Figure 7 illustrates how the sampling of potential solutions for location and severity progresses after 1, 3, 5 and 7 iterations. The x-axis, y-axis and z-axis represent the damage severity, location and probabilistic histogram, respectively, and the dotted markers located in the xy plane indicate the data sampled from the two normal distributions. Distinctively, Figure 7 demonstrates how cross-entropy narrows down the sampling around the exact solution as the iteration number becomes higher. Figure 7(d) shows 500 markers overlapping each other and clustered near the true solution. It is also noticed that the convergence towards the correct severity is achieved more quickly than location. In other words, the objective function is more sensitive to severity than to location.

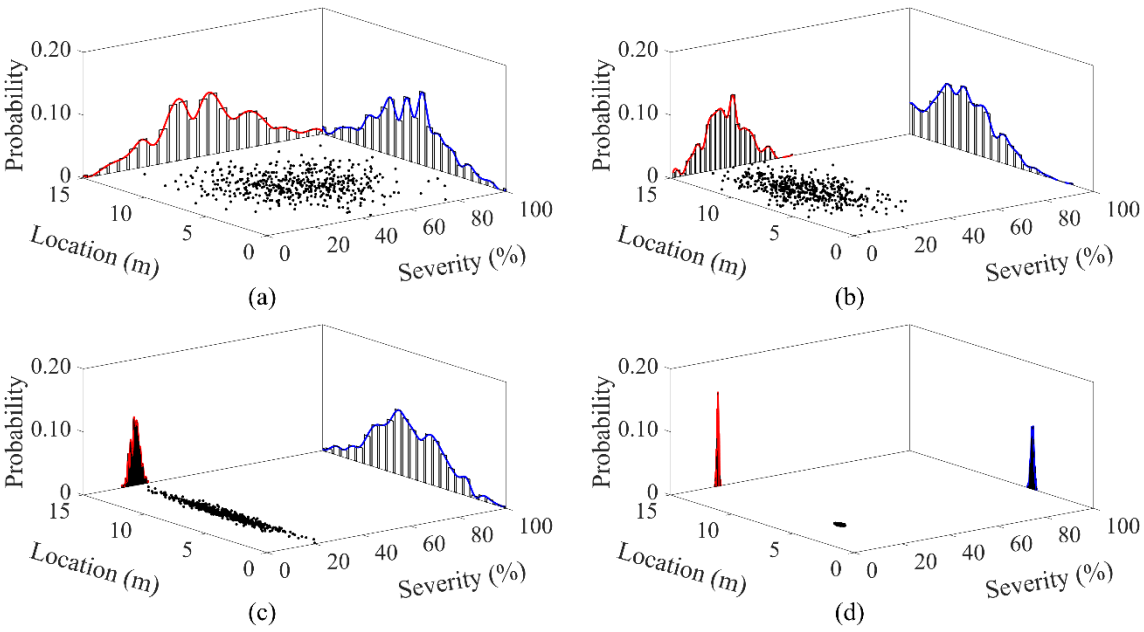

Figure 7. Evolution of sampled solutions with iteration number: (a) 1, (b) 3, (c) 5, (d) 7

6. Influence of number of unknowns and segment position on performance

This section uses as input the acceleration of the unsprung mass of the QC obtained driving at 15 and 30 m/s over the 15 m simply supported bridge with constant stiffness. Therefore, the algorithm, initially unaware that the stiffness is constant, is utilized to estimate the stiffness along the bridge, i.e., the random variables of the cross-entropy procedure are now the stiffness of groups of elementary beams making up the FEM instead of the parameters from Sinha's model as in Section 5. The variation of stiffness along the bridge can be estimated considering a different number of bridge segments, s. For example, s = 1 represents that only one random variable (average bridge stiffness) is considered in the trial FEMs throughout all 150 elementary beams, and s = 2 means that two individual random values of bending stiffness are assigned to the FEMs, i.e., one for each group of 75 elementary beams in the first and second halves of the span. Values of s = 1, 2, 3, 5, 6 and 10, are considered to test the ability of the algorithm in dealing with an increasing number of unknowns. Two different road profiles with geometric spatial means of 0.1×10^{-6} m^3/cycle (class 'A') and 64×10^{-6} m^3/cycle (class 'B') are simulated

to investigate the impact of road roughness.

There is a degree of uncertainty associated with the random sampling that is reduced by repeating the cross-entropy procedure ten times and keeping the average of the final mean values obtained in each repetition. Figure 8 compares the difference between the true and estimated stiffness of the bridge for several beam segments, where the horizontal dashed line in each subfigure indicates the true stiffness, EI (18.46×10^6 kN·m^2). Clearly, s = 1 can provide an excellent match to the average stiffness. When s = 2, 3, 4 or 5, overestimations of stiffness of segments to the left of midspan tend to compensate for underestimations of stiffness of segments to the right. When the number of segments goes up to 6 and 10, inaccurate estimations of stiffness also compensate for each other within half a span.

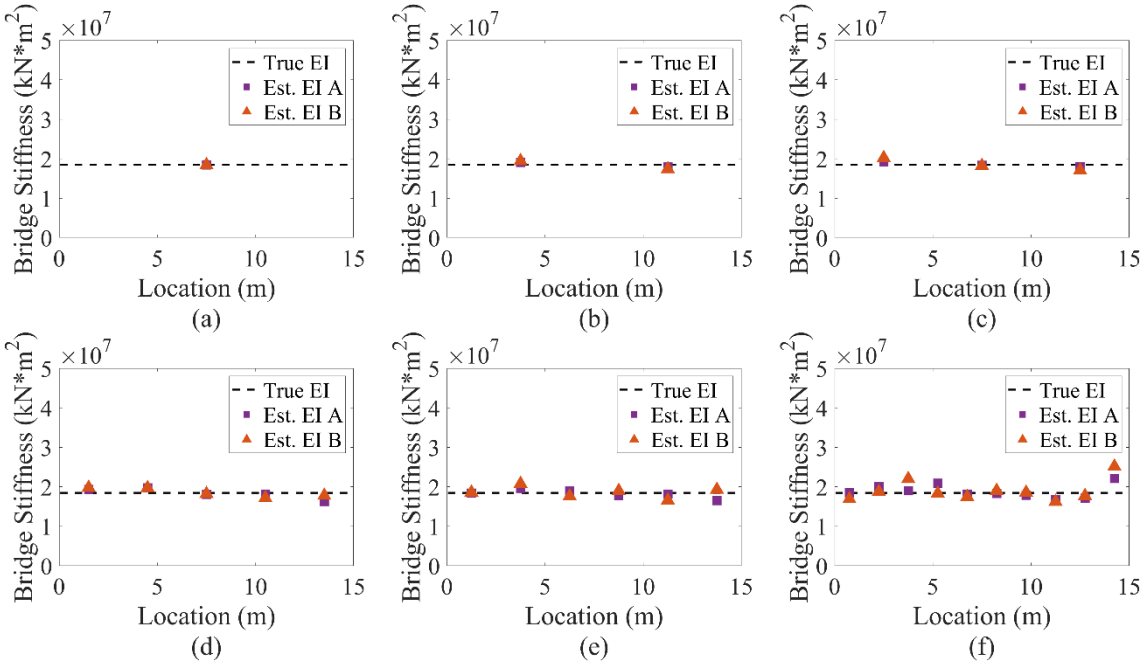

Figure 8. Estimation of stiffness for different number of unknowns of the FEM: (a) s = 1, (b) s = 2, (c) s = 3, (d) s = 5, (e) s = 6, (f) s = 10

The road roughness does not appear to have a significant impact on the results in Figure 8. The largest differences are noticed for s = 10, which is plotted in Figure 9, but this time showing the average and the standard deviation based on the ten solutions from each repetition. For clarity, the markers corresponding to class 'A' and 'B' are spaced slightly, even if they represent the same segment. A closer look allows appreciating that there is a correlation between the accuracy of the stiffness estimation and the standard deviation of the ten repetitions. A narrow standard deviation usually signifies a higher accuracy (i.e., midspan segments), and conversely, a wide standard deviation denotes a higher uncertainty and a poor estimation (i.e., support segments).

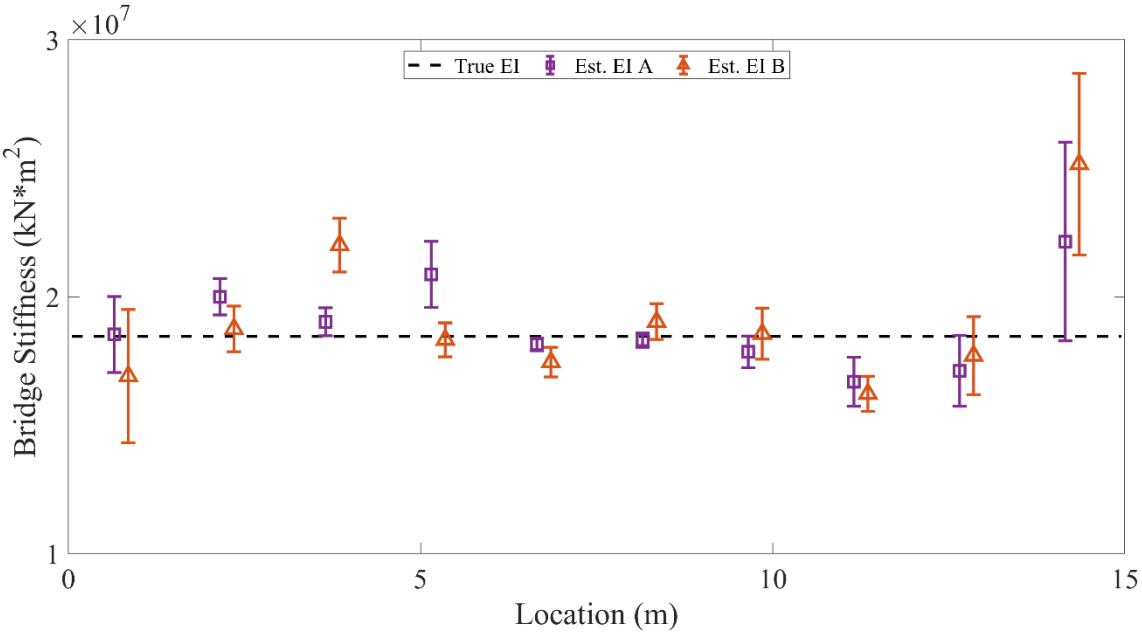

Figure 9. Comparison of average and standard deviation of the estimated stiffness versus true stiffness for 10 segments

Table 2 provides the average of relative errors in estimating the stiffness of the bridge, for FEMs with s = 1, 2, 3, 5, 6 and 10. The relative error in percentage is calculated as the difference between the absolute error (i.e., estimated stiffness of the segment minus true stiffness of the segment) divided by the true value, which is multiplied by 100. If

segments near the supports were discarded, average errors below 7% are found for $s \leq 5$ regardless of the road class. A larger number of unknowns, s = 6 and s = 10, increases the ill-conditioned nature of the problem due to the limited information available. As a result, although the accuracy in the midspan segments [6 - 10.5 m] still looks promising (i.e., average of relative errors below 5.41% for both road classes although there is a higher standard deviation associated with class 'B'), substantial errors can be found in segments next to the supports. Average relative errors of 20.0% and 36.3% are found for the right support segment [13.5 - 15 m] using class 'A' and 'B', respectively. This is somehow expected since the response of the bridge is far more sensitive to changes in stiffness of the segments near midspan than near the supports. Similar conclusions are drawn for road classes 'A' and 'B'.

Table 2. Average of relative errors (%) in stiffness ($\frac{road\ class\ \text{'A'}}{road\ class\ \text{'B'}}$) versus the number of segments (s) (*)

	0.0 - 2.5		2.5 - 5.0		5.0 - 7.5	7.5 - 10.0		10.0 - 12.5		12.5 - 15.0
s = 1					$\frac{0.1}{-0.2}$					
s = 2				$\frac{3.4}{5.4}$			$\frac{-3.0}{-5.7}$			
s = 3		$\frac{3.9}{9.6}$			$\frac{-0.6}{-1.2}$			$\frac{-2.2}{-7.4}$		
s = 5	$\frac{4.6}{7.2}$		$\frac{6.8}{6.8}$		$\frac{-2.0}{-1.3}$		$\frac{-1.7}{-6.9}$		$\frac{-11.6}{-3.7}$	
s = 6	$\frac{-0.4}{0.7}$		$\frac{6.4}{12.6}$		$\frac{2.5}{-4.4}$	$\frac{-3.4}{2.9}$		$\frac{-1.5}{-10.1}$		$\frac{-10.5}{4.6}$
s = 10	$\frac{0.4}{-8.4}$	$\frac{8.4}{1.6}$	$\frac{3.1}{19.3}$	$\frac{13.1}{-0.7}$	$\frac{-1.7}{-5.4}$	$\frac{-0.8}{3.1}$	$\frac{-3.3}{0.6}$	$\frac{-9.5}{-12.1}$	$\frac{-7.3}{-4.0}$	$\frac{20.0}{36.3}$
	0.0 - 1.5	1.5 - 3.0	3.0 - 4.5	4.5 - 6.0	6.0 - 7.5	7.5 - 9.0	9.0 - 10.5	10.5 - 12.0	12.0 - 13.5	13.5 - 15.0

(*) The first and last rows of the table indicate the longitudinal portion of the bridge covered by each segment (m)

7. Estimation of stiffness for damaged bridges

In a general scenario, the overall health condition of the bridge and the damage type will be unknown. Thus, the acceleration of the unsprung mass of the QC while crossing a bridge containing Sinha's damage is used as input to the drive-by algorithm without any prior knowledge about the existence of damage, the damage type or the original stiffness distribution. Four different damage events are assessed: (i) a crack located at 7.5 m with λ = 30%, (ii) a crack located at 5 m with λ = 30%, (iii) a crack located at 7.5 m with λ = 20% and, (iv) a crack located at 5 m with λ = 20%. The FEM is made of 150 elementary beams (Section 3.1), but to simplify the number of unknowns, it is assumed that every consecutive 15 beams have the same stiffness, i.e., s = 10.

Following the steps described in Section 4, Figure 10 shows the average and standard deviation of the estimated stiffness obtained from ten repetitions of the cross-entropy procedure for the four damage scenarios and the two road classes under investigation. The estimated stiffnesses associated with each segment are slightly shifted to improve their visibility. A few remarks can be made about the results:

- The algorithm is successful in capturing the decrease in stiffness corresponding to the crack at 5 m (Figure 10(a)), and at 7.5 m (Figure 10(b)) for both road classes. For instance, a true healthy value of stiffness of 18.46 × 10^6 kN·m^2 decreases within the location range [4.5 - 6 m] of Figure 10(a) to estimated values of 13.65 × 10^6 kN·m^2 for λ = 20% and 10.86 × 10^6 kN·m^2 for λ = 30% using a class 'A' road, and to 12.57 × 10^6 kN·m^2 (λ = 20%) and 10.73 × 10^6 kN·m^2 (λ = 30%) using a class 'B' road.

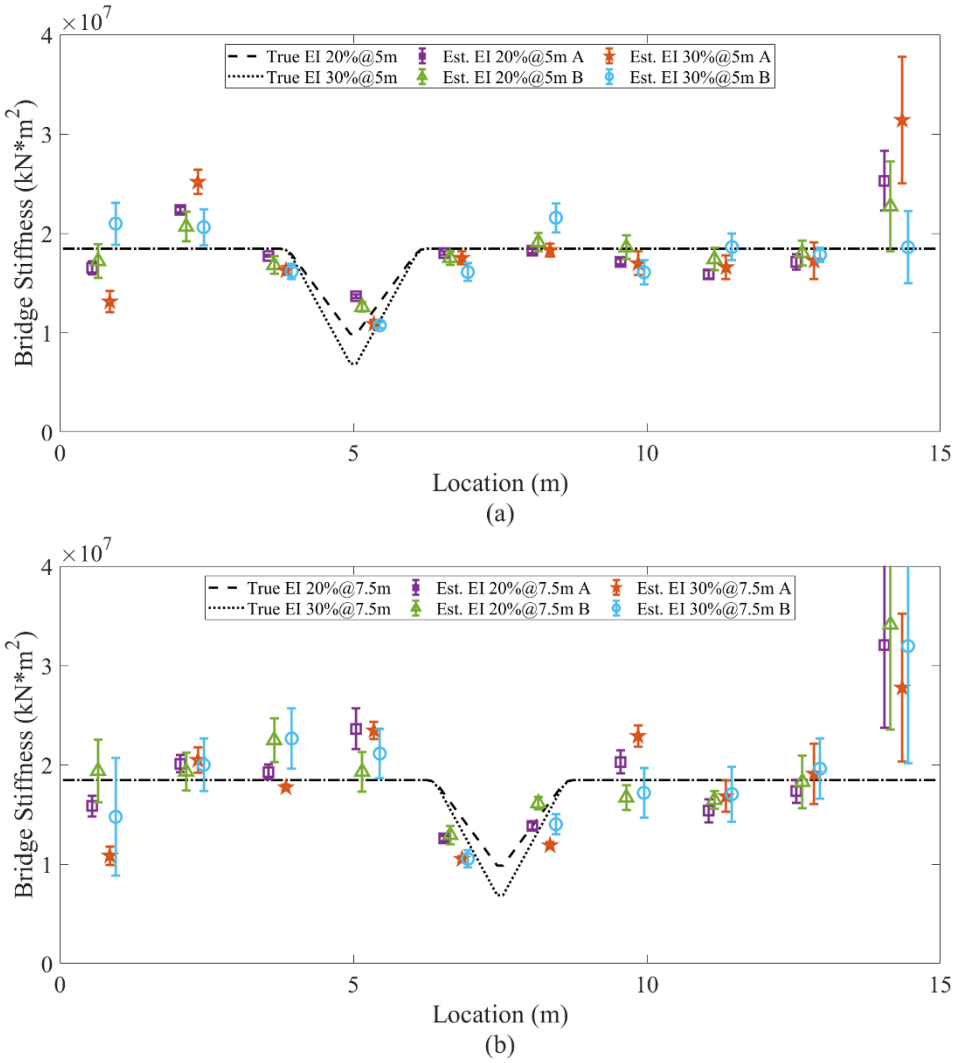

Figure 10. Estimation of stiffness profiles based on 10 repetitions of the cross-entropy procedure for cracks (λ = 20% and 30%) located at: (a) 5 m, (b) 7.5 m

- A considerable loss of accuracy takes place in the segment next to the supports, more noticeably the right support, for all damage events and both road classes. This error is unavoidable due to the reduced contribution of the end segments to the overall response. Since the stiffness of segment 10 next to the right support is overestimated in most scenarios, as a consequence, the stiffness in segments 9 and 8 tends to be underestimated to compensate for that error.

- Broadly speaking, a narrow standard deviation seems to correlate with a higher accuracy of the average value proposed as the solution. From analysing the figures, the errors are smaller at the crack or nearby, which agrees with a smaller value of the standard deviation compared to other locations. The latter is a relevant output of the cross-entropy procedure given that the solution appears to offer a measure of its reliability. Nonetheless, this is not a definitive rule, particularly for segments far apart from midspan, where outliers are more likely, i.e., isolated points giving a very accurate solution with a high standard deviation or a poor solution with a small standard deviation.
- Increasing the road roughness causes an increase in uncertainty as denoted by the larger standard deviations of class 'B' results compared to class 'A'. The best estimations of stiffness using a class 'B' road are found at the crack location where the standard deviations are also smaller.

Figure 11 gives the absolute values of the relative errors (%) in estimating stiffness versus the coefficient of variation (CoV = standard deviation/mean) using all segments of Figures 10(a) and 10(b), i.e., forty scenarios for each road profile. The largest errors (> 50%) are found for CoVs above 0.2, and they correspond to segments next to the supports. As expected, the CoV tends to be higher for the class 'B' road. Nonetheless, only two predictions with the class 'B' road result in a relative error above 25% compared to nine predictions with the road class 'A'. Thus, a linear regression model yields a lower slope for the class 'B' profile. A close look at the lowest CoV range [0 - 0.05] allows finding a total of seven predictions using a road class 'B', all of them with an error < 10%. Within the same CoV range [0 - 0.05], it is possible to find twenty-three predictions using a class 'A' road, fourteen of which have an error < 10%. Overall, results associated with a high

CoV should be mistrusted, whereas those with a low CoV usually imply less scatter and a more reliable estimation of the stiffness, even more in the case of the rougher profile.

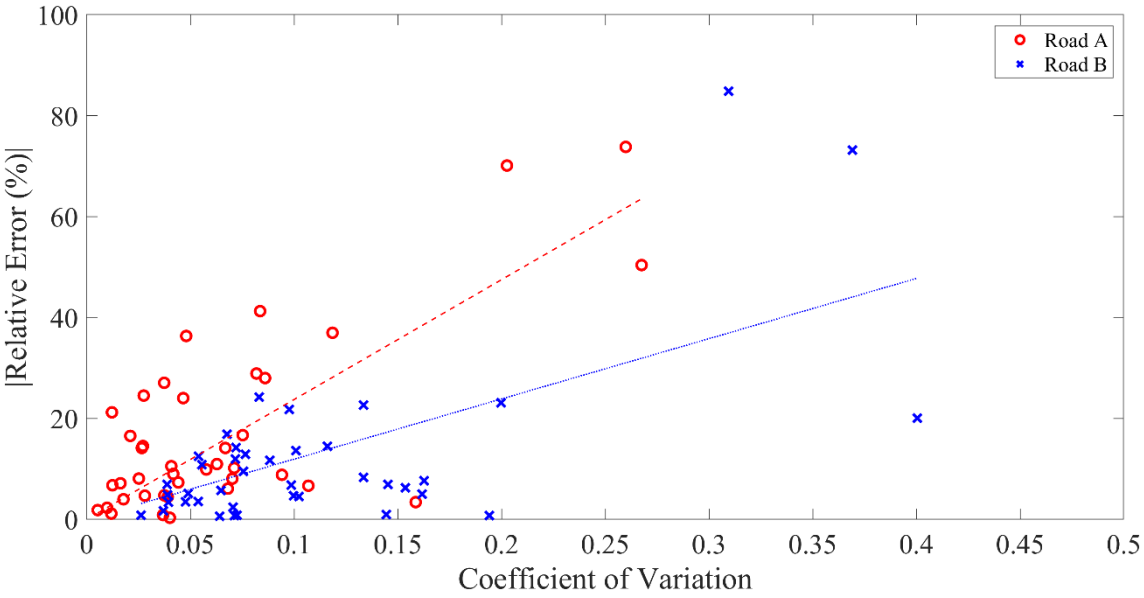

Figure 11. Absolute values of the relative error (%) versus coefficient of variation

8. Influence of bridge damping, speed and transverse variations of the vehicle

For the sake of computational efficiency, the new simulations in this section utilize a FEM of the bridge consisting of 30 beam elements. The same road class 'B' employed in Sections 6 and 7 is used to test four combinations of speeds: 15 and 30 m/s, 10 and 15 m/s, 10 and 20 m/s, 10 and 30 m/s. Figures 12(a) and (b) give the stiffness profile estimated for a crack with λ = 30% and λ = 20%, respectively, located at 5 m.

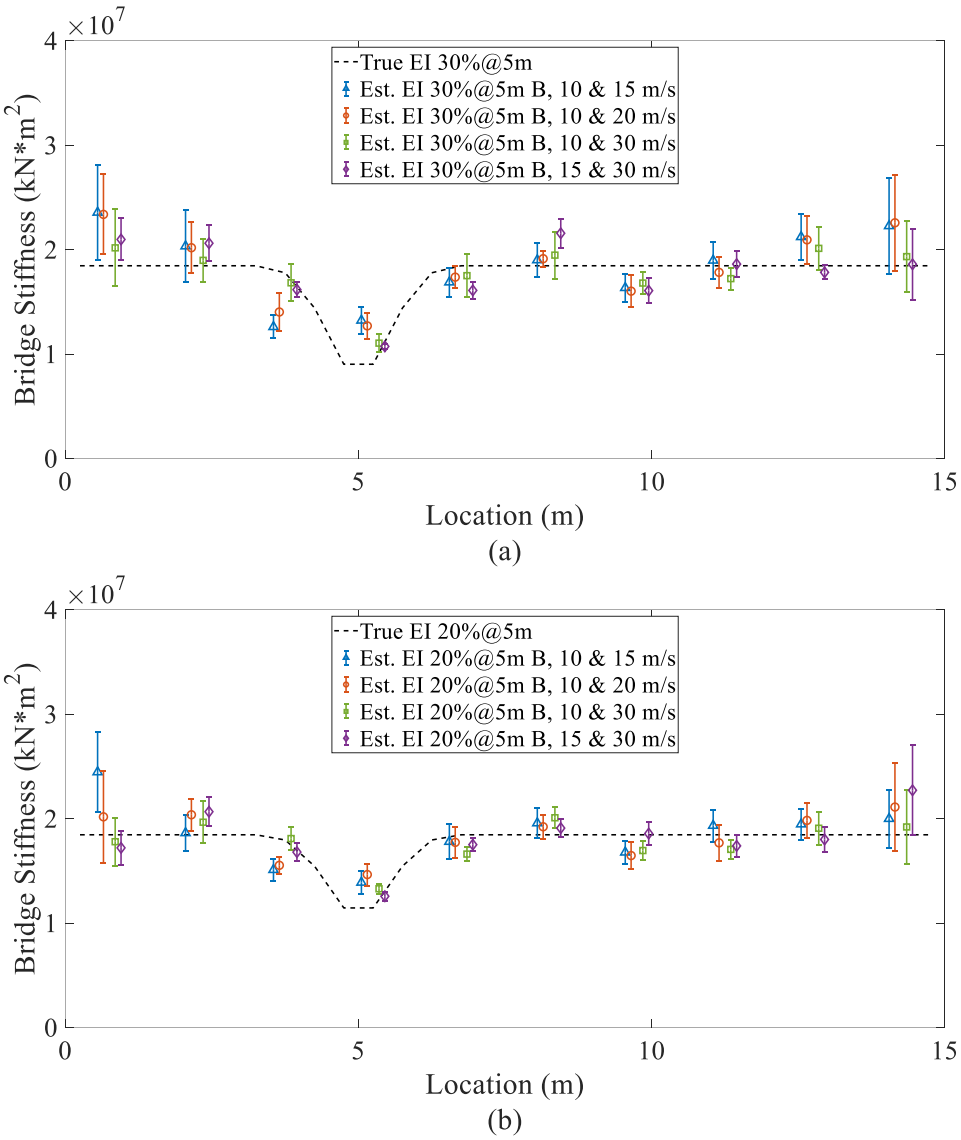

Figure 12. Estimation of stiffness profiles based on 10 repetitions of the cross-entropy procedure for four combinations of speed and crack located at 5 m with severity: (a) λ = 30%, (b) λ = 20%

Tables 3 and 4 provide the average and standard deviation of relative errors (%) in stiffness due to the 10 repetitions of the cross-entropy procedure for each of the 10 segments in both damage scenarios. If unreliable predictions near the supports are ignored, the most accurate results are obtained using the combinations (10,30) and (15,30). The objective function (Equation (16)) normalised by the total number R of

locations along the road profile being compared, can be used as a reference for a preliminary assessment of the overall accuracy of each combination of speeds. For example, the damage scenario with λ = 30% and speed combinations of (15,30), (10,15), (10,20) and (10,30) lead to average values of the normalised objective function (considering the 10 cross-entropy runs) of 2.29×10^{-6} m ($\sigma = 1.62 \times 10^{-8}$ m), 4.42×10^{-7} m ($\sigma = 4.24 \times 10^{-8}$ m), 9.59×10^{-7} m ($\sigma = 1.10 \times 10^{-7}$ m) and 2.80×10^{-6} m ($\sigma = 3.19 \times 10^{-8}$ m), respectively.

Table 3. Average (μ) and standard deviation (σ) of relative errors (%) in stiffness for λ = 30% at 5 m, and four speed combinations (v_1, v_2) on a class 'B' road

Segment location (m)	0.0 - 1.5	1.5 - 3.0	3.0 - 4.5	4.5 - 6.0	6.0 - 7.5	7.5 - 9.0	9.0 - 10.5	10.5 - 12.0	12.0 - 13.5	13.5 - 15.0
μ(σ) for (15,30)	13.6 (10.9)	11.7 (9.3)	−4.2 (4.4)	−0.8 (2.5)	−11.7 (4.5)	16.9 (7.5)	−12.9 (6.3)	0.9 (6.9)	−3.4 (3.6)	0.8 (18.6)
μ(σ) for (10,15)	27.6 (24.9)	10.2 (18.6)	−25.4 (6.6)	22.2 (12.3)	−7.4 (7.6)	2.9 (8.8)	−11.5 (7.1)	2.8 (9.8)	15.0 (11.8)	20.6 (25.1)
μ(σ) for (10,20)	26.6 (20.7)	9.4 (13.2)	−16.9 (10.5)	17.3 (11.4)	−4.7 (5.6)	3.7 (4.1)	−13.2 (8.4)	−3.4 (8.2)	13.4 (12.6)	22.3 (24.8)
μ(σ) for (10,30)	9.3 (20.0)	2.8 (11.0)	−0.4 (10.5)	2.1 (7.7)	−4.0 (11.2)	5.5 (12.2)	−9.0 (5.9)	−6.7 (5.8)	9.0 (11.3)	4.7 (18.3)

Table 4. Average (μ) and standard deviation (σ) of relative errors (%) in stiffness for λ = 20% at 5 m, and four speed combinations (v_1, v_2) on a class 'B' road

Segment location (m)	0.0 - 1.5	1.5 - 3.0	3.0 - 4.5	4.5 - 6.0	6.0 - 7.5	7.5 - 9.0	9.0 - 10.5	10.5 - 12.0	12.0 - 13.5	13.5 - 15.0
μ(σ) for (15,30)	−6.8 (8.7)	12.0 (7.6)	−2.8 (5.0)	−1.7 (3.5)	−4.3 (3.5)	3.5 (4.7)	0.6 (6.1)	−5.8 (5.8)	−2.4 (6.5)	23.1 (23.3)
μ(σ) for (10,15)	32.5 (20.7)	0.9 (9.6)	−12.6 (6.0)	8.6 (8.6)	−2.7 (9.0)	6.0 (7.8)	−9.1 (5.9)	4.7 (8.3)	5.5 (8.0)	8.3 (15.1)
μ(σ) for (10,20)	9.3 (24.0)	10.4 (8.4)	−10.2 (4.8)	14.6 (8.3)	−3.1 (8.0)	4.2 (6.2)	−10.8 (7.1)	−4.2 (9.2)	7.5 (8.9)	14.4 (22.8)
μ(σ) for (10,30)	−3.6 (12.5)	6.5 (10.9)	4.7 (6.3)	3.9 (3.6)	−9.2 (3.7)	8.8 (5.4)	−8.2 (4.9)	−7.6 (5.0)	3.4 (8.6)	4.1 (19.2)

The transverse position of the vehicle is not expected to vary significantly between runs once the driver is instructed to follow a predetermined path, however, a degree of uncertainty remains. This uncertainty can be reduced by increasing the number of runs, using vision-based tracking, or monitoring the objective function. Differences of 0.05, 0.10 and 0.15 m in transverse location between the two speeds are adopted to assess the impact of travelling along different wheel paths. Based on the real-valued cross-spectra of a Gaussian road surface (Cebon & Newland, 1983), Figures 13(a), (b) and (c) show the correlated track profiles for 2.3 m corresponding to the middle portion of a lane with a class 'B' road profile ($G_d(n_0)$= 64 × 10^{-6} m^3/cycle). The distance between the left and right wheels is adopted to be 1.80 m. Four transverse positions of the vehicle are considered: driving in the centreline of the lane, and 0.05 m, 0.10 m, and 0.15 m to the left from this centreline. Figures 13(b) and (c) signal the four paths of the vehicle employed in the analysis. The one-dimensional profiles to be used in the QC simulations, shown in Figure 13(d), are computed from the average of the irregularities corresponding to the smoothed left and the right wheel-track profiles (Sayers & Karamihas, 1996). Given that the contact between the vehicle and the road extends over the contact patch of the tyre, a moving average filter with a base length of 0.24 m (González & Mohammed, 2019; Liang et al., 2013) is incorporated within the carpet of Figure 13 to remove shorter wavelength disturbances.

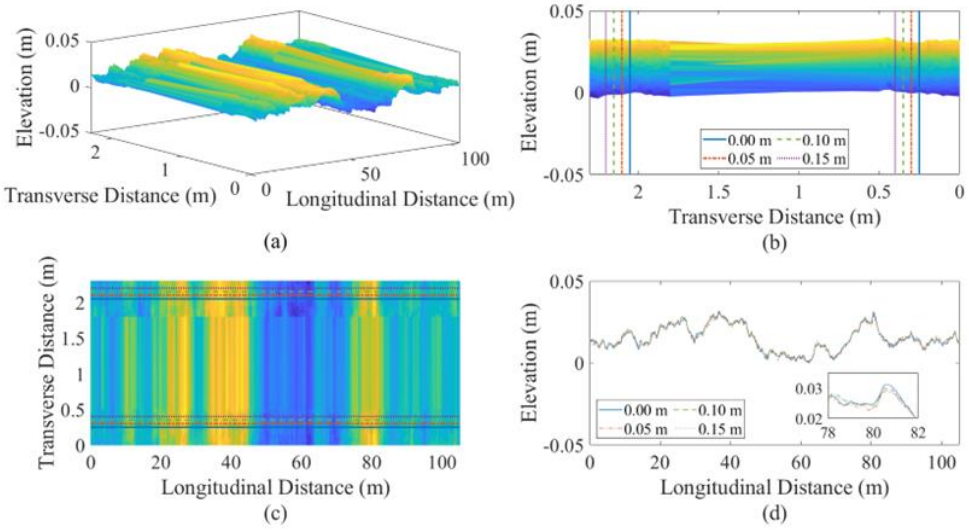

Figure 13. Transverse variation of road irregularities for an ISO class 'B': (a) Perspective view of road carpet, (b) elevation vs transverse distance, (c) contour plot of elevation vs transverse and longitudinal distances, (d) profiles employed in QC simulations

Figure 14 and Table 5 present the average and standard deviation of the estimated stiffness and relative errors respectively, for the class 'B' carpet in Figure 13, and for a class 'A' carpet ($G_d(n_0)$= 0.1 × 10^{-6} m^3/cycle). The true stiffness profile corresponds to damage event (ii) consisting of the crack (λ = 30%) located at 5 m, and four testing scenarios with the vehicle travelling at 15 m/s on the centreline, and at 30 m/s on the following path: (ii-1) the centreline, (ii-2) 0.05 m to the left of the centreline, (ii-3) 0.10 m to the left of the centreline, and (ii-4) 0.15 m to the left of the centreline. Clearly, differences in the transverse position of the vehicle at the two speeds have a negative impact on the performance of the proposed algorithm, the more detrimental the rougher the profile. The objective function can be used to accept or reject the stiffness estimation by a particular pair of runs. For example, the normalised objective function adopts average values of 2.35 × 10^{-7} m (σ = 2.21 × 10^{-8} m), 1.55 × 10^{-6} m (σ = 1.32 × 10^{-8} m),

1.66×10^{-6} m ($\sigma = 1.15 \times 10^{-8}$ m) and 1.58×10^{-6} m ($\sigma = 3.47 \times 10^{-9}$ m), for differences in transverse location between runs corresponding to 0, 0.05, 0.10 and 0.15 m respectively. As expected, the best results (i.e., the objective function is about one order of magnitude less) are obtained when the vehicle drives over the same wheel path for both speeds. The discrepancies become more significant with the rougher 'B' profile, where the normalised objective function has average values of 9.44×10^{-6} m ($\sigma = 3.68 \times 10^{-7}$ m), 2.38×10^{-5} m ($\sigma = 1.86 \times 10^{-8}$ m), 3.73×10^{-5} m ($\sigma = 3.02 \times 10^{-8}$ m) and 4.75×10^{-5} m ($\sigma = 1.61 \times 10^{-7}$ m), for differences in the transverse location corresponding to 0, 0.05, 0.10 and 0.15 m respectively.

Table 5. Average (μ) and standard deviation (σ) of relative errors (%) in stiffness for λ = 30% at 5 m, travelling at 15 and 30 m/s on four different wheel paths of class 'A' and 'B' road carpets

Segment location (m)	0.0 - 1.5	1.5 - 3.0	3.0 - 4.5	4.5 - 6.0	6.0 - 7.5	7.5 - 9.0	9.0 - 10.5	10.5 - 12.0	12.0 - 13.5	13.5 - 15.0
μ(σ) for (ii-1), 'A'	−15.8 (8.3)	22.9 (1.5)	−10.5 (0.4)	−0.4 (2.3)	0.5 (5.2)	3.7 (3.7)	−7.7 (1.6)	−17.0 (2.5)	22.6 (8.0)	121.3 (48.8)
μ(σ) for (ii-1), 'B'	81.7 (23.3)	28.8 (22.7)	−16.2 (9.8)	8.2 (9.7)	−10.4 (8.9)	11.3 (11.5)	−0.4 (7.0)	−8.5 (4.3)	−8.3 (7.5)	52.8 (50.2)
μ(σ) for (ii-2), 'A'	110.8 (21.8)	−20.4 (0.8)	−12.4 (1.1)	−3.4 (1.0)	−19.8 (1.4)	4.2 (2.7)	63.8 (16.8)	68.6 (15.2)	−51.5 (3.1)	−60.2 (8.3)
μ(σ) for (ii-2), 'B'	−67.9 (4.8)	−6.0 (12.9)	−54.2 (2.0)	51.5 (16.5)	0.9 (14.5)	−31.3 (5.0)	−7.0 (7.7)	39.9 (15.2)	52.8 (12.5)	63.4 (28.0)
μ(σ) for (ii-3), 'A'	79.8 (19.5)	4.4 (1.4)	−7.1 (1.4)	8.0 (2.1)	−18.8 (2.9)	−8.2 (3.4)	15.6 (7.7)	39.2 (24.7)	−38.6 (8.8)	−53.1 (12.8)
μ(σ) for (ii-3), 'B'	−73.0 (7.9)	50.1 (16.7)	−72.5 (0.7)	−19.8 (5.1)	37.3 (16.5)	119.3 (13.0)	110.7 (18.6)	71.2 (14.4)	5.7 (13.0)	−7.4 (12.7)
μ(σ) for (ii-4), 'A'	159.2 (23.8)	−11.6 (1.9)	−5.7 (1.5)	3.1 (1.5)	−28.0 (1.9)	2.2 (4.4)	25.8 (8.8)	57.7 (20.7)	−47.5 (3.6)	−1.4 (17.8)
μ(σ) for (ii-4), 'B'	−94.0 (2.5)	−52.6 (18.7)	71.4 (21.1)	−52.7 (5.7)	−60.4 (6.9)	141.0 (31.5)	133.8 (27.0)	114.4 (21.0)	84.9 (41.3)	35.5 (32.8)

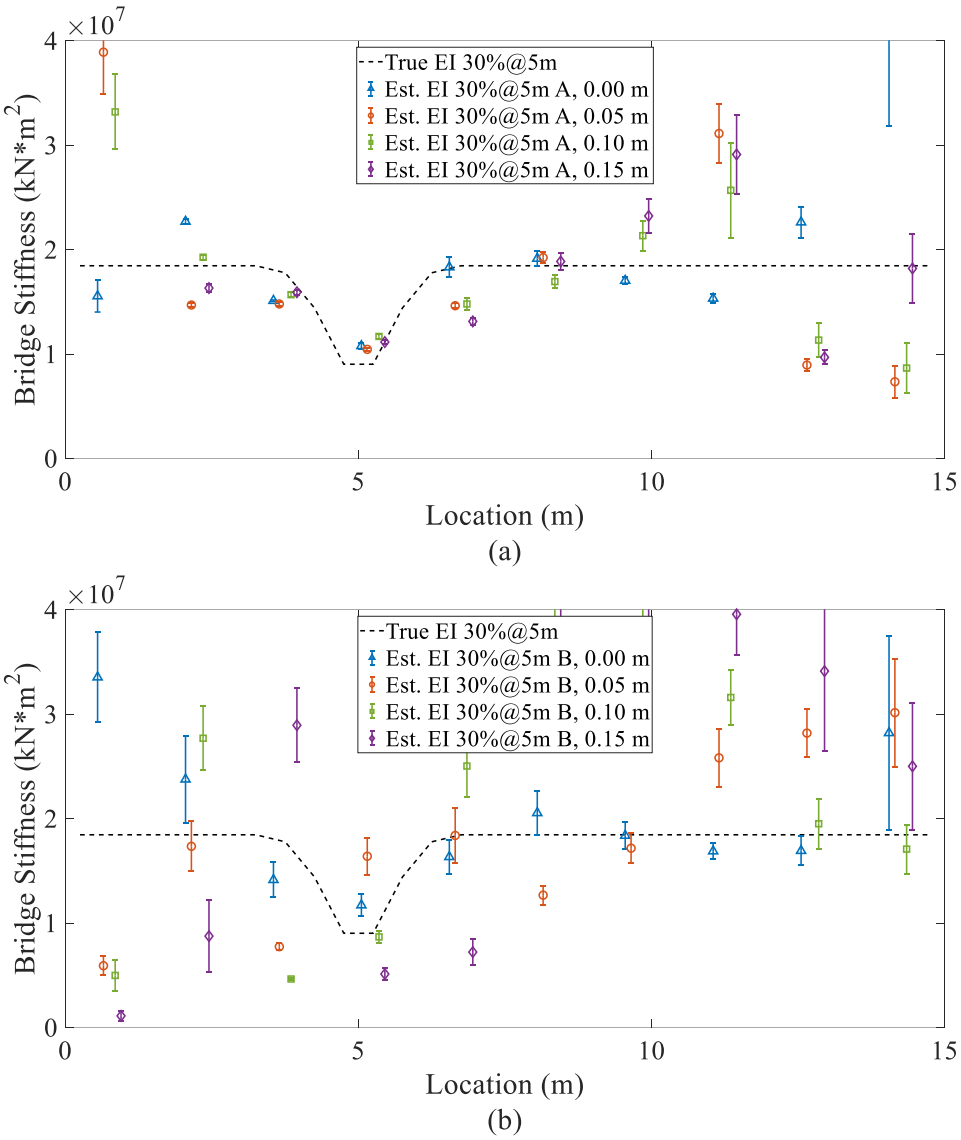

Figure 14. Estimation of stiffness profiles based on 10 repetitions of the cross-entropy procedure for crack (λ = 30%) located at 5 m, under four different wheel paths of a road carpet falling within: (a) class 'A', (b) class 'B'

Following ambient vibration measurements of 114 highway bridges in China, Li et al. (2014) recommend damping ratios ζ of 3.5%, 4%, 2.5% and 2.5% for the first mode of simply supported, continuous, arch and continuous rigid-frame reinforced concrete bridges respectively. The low values of bridge damping are expected to have a minor impact due to two main reasons: (1) in forced vibration, the total bridge response is made of both static and dynamic components, with damping only affecting the dynamic component, which is usually also the smallest one and, (2) the slight disparities between

undamped (f_1) and damped frequencies (i.e., for $\zeta = 3.5\%$, $f_{1,d} \approx 0.9994 f_1$), combined with the short duration of vehicle crossings, which will lead to tiny differences between the undamped and damped drive-by measurements.

Drive-by measurements are simulated using the one-dimensional class 'B' road profile from Sections 6 and 7 at 15 and 30 m/s for a bridge with a crack located at 5 m with λ = 30%, but $\zeta = 3.5\%$ modelled using Rayleigh damping. The bridge damping (ζ) is added to the bridge model and integrated within the optimization loop as an additional unknown together with the bending stiffness of elementary bridge elements, i.e., a total of 11 unknowns. The optimisation leads to an average ζ value of 4.79% with a standard deviation of 0.45%, and to ten values of average and standard deviation for the stiffness of the segments as plotted in Figure 15. For comparison purposes, this figure also provides the results for the same parameters of vehicle, road, bridge and damage, but zero damping assumed to be known (i.e., as in Figure 10(a)).

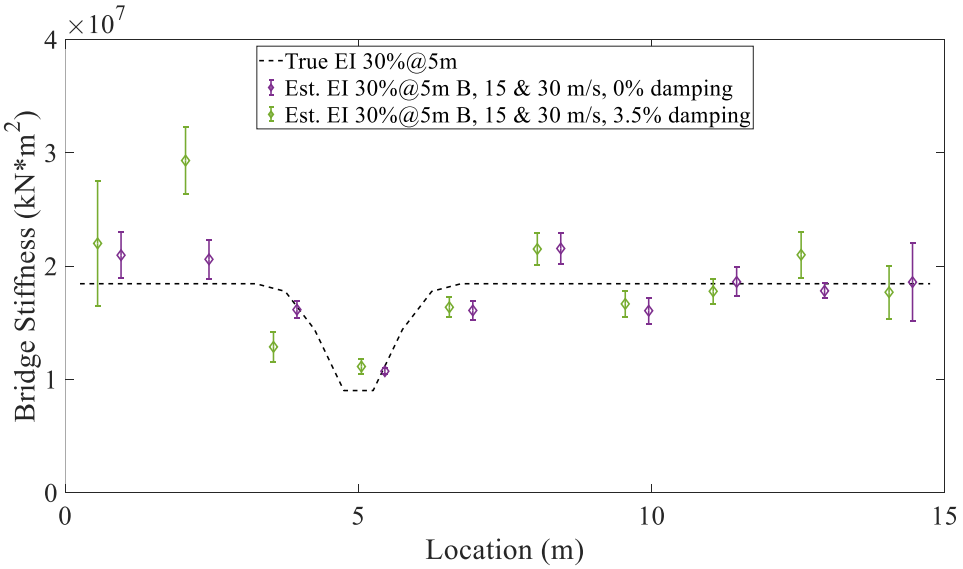

Figure 15. Estimation of stiffness profiles based on 10 repetitions of the cross-entropy procedure for crack (λ = 30%) located at 5 m, under two scenarios: a known 0% damping and an unknown 3.5% damping

Although the introduction of a new uncertainty increases inaccuracy, the relative errors in Table 6 show how, away from the first support, the algorithm is able to characterize the stiffness with a similar degree of accuracy.

Table 6. Average (μ) and standard deviation (σ) of relative errors (%) in stiffness for λ = 30% at 5 m, travelling at 15 and 30 m/s on a class 'B' road, with two damping scenarios: a known 0% damping, and an unknown 3.5% damping

Segment location (m)	0.0 - 1.5	1.5 - 3.0	3.0 - 4.5	4.5 - 6.0	6.0 - 7.5	7.5 - 9.0	9.0 - 10.5	10.5 - 12.0	12.0 - 13.5	13.5 - 15.0
μ(σ) for known $\zeta = 0\%$	13.6 (10.9)	11.7 (9.3)	−4.2 (4.4)	−0.8 (2.5)	−11.7 (4.5)	16.9 (7.5)	−12.9 (6.3)	0.9 (6.9)	−3.4 (3.6)	0.8 (18.6)
μ(σ) for unknown $\zeta = 3.5\%$	19.3 (30.0)	58.9 (16.1)	−23.7 (7.9)	3.0 (6.4)	−10.2 (4.9)	16.6 (7.5)	−9.7 (6.3)	−3.6 (6.1)	13.8 (11.0)	−4.1 (12.7)

9. Conclusions

In contrast to the traditional level I drive-by based approaches for SHM of bridges, which detect, but do not locate or quantify damage, this paper has proposed a model-based level III drive-by algorithm. Unlike preceding drive-by methods, results are not affected by changes in the road profile with time or by the need for a baseline reference from a time when the bridge was deemed to be healthy. The proposed algorithm has successfully reduced the undesired components due to the dynamics of the vehicle and road irregularities that commonly hinder the damage. Even in challenging scenarios with speeds of 30 m/s, and a rough road class 'B', the algorithm has been able to detect, locate and quantify a stiffness loss while also providing a method for road profiling on the bridge. Although the extraction of the road profile has not been the main objective of the

paper, this feature cannot be underrated. The roughness of a road profile on the bridge and the approach to the bridge is acknowledged to be a major cause of dynamic amplification of the forces in a vehicle, and it can lead to a significant increment of the response of the bridge.

Nearly as significant as the ability to locate and quantify damage, is the possibility of assessing the reliability of the proposed solution through the standard deviation. A low CoV has been shown to represent a better estimation of the true stiffness for a significant proportion of the tested segments. If the bridge was traversed by several vehicles simultaneously, the proposed methodology would not work unless all the axle forces and the locations of their point of application on the bridge were known at each point in time. Therefore, the proposed methodology is best suited for short and medium span bridges, where single-vehicle events are easier to achieve. For instance, the instrumented vehicle could take measurements in times of reduced traffic or be accompanied by a police escort that guaranteed a minimum inter-vehicle distance.

As a suggestion for further research, the algorithm needs to be assessed using field measurements and a three-dimensional bridge model. The stiffness of this model will vary longitudinally and transversely, which will increase the number of unknowns considerably. To reduce the uncertainty associated with these unknowns, the path of the vehicle can be varied to gather more information about the bridge, i.e., using several runs of the vehicle travelling at different transverse locations for each speed. In fact, what the algorithm would be minimizing for would be a road carpet surface. Additionally, the sensitivity of the algorithm to the selected values of speed must be investigated. Theoretical developments are currently preceding technological advances in the drive-by SHM field. Therefore, testing of drive-by algorithms with field measurements is strongly needed to evaluate the impact on the performance of the accuracy of measuring devices,

the noise in the measurements or the discrepancies between the numerical models and reality. Although these factors are expected to lead to somewhat worse results than reported in this paper, improvements in measurement technology, noise filtering and digital-twin modelling should contribute to closing the gap between numerical simulations and field validation.

Acknowledgements

This research has received funding from Science Foundation Ireland (SFI)'s US-Ireland R&D partnership programme under the proposal id. 16/US/I3277 titled MARS-Fly.

Disclosure statement

No potential conflict of interest was reported by the author(s).

References

Agostinacchio, M., Ciampa, D., & Olita, S. (2014). The vibrations induced by surface irregularities in road pavements - a Matlab® approach. *European Transport Research Review*, *6*(3), 267–275. https://doi.org/10.1007/s12544-013-0127-8

Alves, V., & Cury, A. (2021). A fast and efficient feature extraction methodology for structural damage localization based on raw acceleration measurements. *Structural Control and Health Monitoring*, *28*(7), Article 2748. https://doi.org/10.1002/stc.2748

Barbosa, R. S. (2011). Vehicle dynamic safety in measured rough pavement. *Journal of Transportation Engineering*, *137*(5), 305–310. https://dx.doi.org/10.1061/(ASCE)TE.1943-5436.0000216

Camara, A., Vázquez, V. F., Ruiz-Teran, A. M., & Paje, S. E. (2017). Influence of the pavement surface on the vibrations induced by heavy traffic in road bridges. *Canadian Journal of Civil Engineering*, *44*(12), 1099–1111. https://doi.org/10.1139/cjce-2017-0310

Cebon, D., & Newland, D. E. (1983). Artificial generation of road surface topography by the inverse F.F.T. method. *Vehicle System Dynamics*, *12*(1–3), 160–165. https://doi.org/10.1080/00423118308968747

Chai, G., Manoharan, S., Golding, A., Kelly, G., & Chowdhury, S. (2016). Evaluation of the traffic speed deflectometer data using simplified deflection model. *Transportation Research Procedia*, *14*, 3031–3039. https://dx.doi.org/10.1016/j.trpro.2016.05.444

Chen, Z. W., Cai, Q. L., & Zhu, S. (2018). Damage quantification of beam structures using deflection influence lines. *Structural Control and Health Monitoring*, *25*(11), Article 2242. https://doi.org/10.1002/stc.2242

Corbally, R., & Malekjafarian, A. (2021). Examining changes in bridge frequency due to damage using the contact-point response of a passing vehicle. *Journal of Structural Integrity and Maintenance*, *6*(3), 148–158. https://doi.org/10.1080/24705314.2021.1906088

Domaneschi, M., Pellecchia, C., De Iuliis, E., Cimellaro, G. P., Morgese, M., Khalil, A. A., & Ansari, F. (2020). Collapse analysis of the Polcevera viaduct by the applied element method. *Engineering Structures*, *214*, Article 110659. https://doi.org/10.1016/j.engstruct.2020.110659

Dowling, J., OBrien, E. J., & González, A. (2012). Adaptation of cross entropy optimisation to a dynamic bridge WIM calibration problem. *Engineering Structures*, *44*, 13–22. https://doi.org/10.1016/j.engstruct.2012.05.047

Elhattab, A., Uddin, N., & OBrien, E. J. (2016). Drive-by bridge damage monitoring using bridge displacement profile difference. *Journal of Civil Structural Health Monitoring*, *6*(5), 839–850. https://doi.org/10.1007/s13349-016-0203-6

Engineering News-Record. (2019, November 20). *Fatal fall: Two motorists killed as suspension bridge collapses in France*. ENR. https://www.enr.com/articles/48180-two-motorists-killed-as-suspension-bridge-collapses-in-france.

Fernando, E., Harrison, G., & Hilbrich, S. (2007). *Truck instrumentation for dynamic load measurement* (Report No. FHWA/TX-06/0-4863-1). Texas Transportation Institute, The Texas A&M University System.

Garrido, H., Domizio, M., Curadelli, O., & Ambrosini, D. (2020). Numerical, statistical and experimental investigation on damage quantification in beams from modal curvature. *Journal of Sound and Vibration*, *485*, Article 115591. https://doi.org/10.1016/j.jsv.2020.115591

González, A. (2010). Vehicle-bridge dynamic interaction using finite element modelling. In D. Moratal (Ed.), *Finite element analysis* (pp. 637–662). IntechOpen. https://doi.org/10.5772/10235

González, A., & Mohammed, O. (2019). Damage detection in bridges based on patterns of dynamic amplification. *Structural Control and Health Monitoring*, 2*6*(7), Article 2361. https://doi.org/10.1002/stc.2361

González, A., OBrien, E. J., Li, Y. Y., & Cashell, K. (2008). The use of vehicle acceleration measurements to estimate road roughness. *Vehicle System Dynamics*, *46*(6), 483–499. https://dx.doi.org/10.1080/00423110701485050

Green, M. F., & Cebon, D. (1994). Dynamic response of highway bridges to heavy vehicle loads: Theory and experimental validation. *Journal of Sound and Vibration*, *170*(1), 51–78. https://doi.org/10.1006/jsvi.1994.1046

Harris, N. K., González, A., OBrien, E. J., & McGetrick, P. J. (2010). Characterisation of pavement profile heights using accelerometer readings and a combinatorial optimisation technique. *Journal of Sound and Vibration*, *329*(5), 497–508. https://doi.org/10.1016/j.jsv.2009.09.035

He, W.Y., He, J., & Ren, W.X. (2019). The use of mode shape estimated from a passing vehicle for structural damage localization and quantification. *International Journal of Structural Stability and Dynamics*, *19*(10), Article 1950124. https://doi.org/10.1142/S0219455419501244

He, W. Y., Ren, W. X., & Zuo, X. H. (2018). Mass-normalized mode shape identification method for bridge structures using parking vehicle-induced frequency change. *Structural Control and Health Monitoring*, *25*(6), Article 2174. https://doi.org/10.1002/stc.2174

Hester, D., & González, A. (2015). A bridge-monitoring tool based on bridge and vehicle accelerations. *Structure and Infrastructure Engineering*, *11*(5), 619–637. https://doi.org/10.1080/15732479.2014.890631

Hester, D., & González, A. (2017). A discussion on the merits and limitations of using drive-by monitoring to detect localised damage in a bridge. *Mechanical Systems and Signal Processing*, *90*, 234–253. https://doi.org/10.1016/j.ymssp.2016.12.012

International Organization for Standardization. (2016). *Mechanical vibration - Road surface profiles - Reporting of measured data* (ISO 8608:2016).

Karnopp, D. (2009). How significant are transfer function relations and invariant points for a quarter car suspension model? *Vehicle System Dynamics*, *47*(4), 457–464. https://doi.org/10.1080/00423110802179909

Keenahan, J., & OBrien, E. J. (2018). Drive-by damage detection with a TSD and time-shifted curvature. *Journal of Civil Structural Health Monitoring*, *8*(3), 383–394. https://doi.org/10.1007/s13349-018-0280-9

Keenahan, J., Ren, Y. F., & OBrien, E. J. (2019). Determination of road profile using multiple passing vehicle measurements. *Structure and Infrastructure Engineering*, *16*(9), 1262–1275. https://doi.org/10.1080/15732479.2019.1703757

Kim, C. W., Chang, K. C., McGetrick, P. J., Inoue, S., & Hasegawa, S. (2017). Utilizing moving vehicles as sensors for bridge condition screening: A laboratory verification. *Sensors and Materials*, *29*(2), 153–163. https://dx.doi.org/10.18494/SAM.2017.1433

Li, J. T., Zhu, X. Q., Law, S. S., & Samali, B. (2019). Drive-by blind modal identification with singular spectrum analysis. *Journal of Aerospace Engineering*, *32*(4), Article 04019050. https://doi.org/10.1061/(ASCE)AS.1943-5525.0001030

Li, P. F., Wang, Y. F., Liu, B. D., & Su, L. (2014). Damping properties of highway bridges in China. *Journal of Bridge Engineering*, *19*(5), Article 04014005. https://doi.org/10.1061/(ASCE)BE.1943-5592.0000578

Liang, C., Wang, G., An, D., & Ma, Y. (2013). Tread wear and footprint geometrical characters of truck bus radial tires. *Chinese Journal of Mechanical Engineering*, *26*, 506–511. https://doi.org/10.3901/CJME.2013.03.506

Lin, C. W., & Yang, Y. B. (2005). Use of a passing vehicle to scan the fundamental bridge frequencies: An experimental verification. *Engineering Structures*, *27*(13), 1865–1878. https://doi.org/10.1016/j.engstruct.2005.06.016

Liu, C. Y., Zhu, Y. P., & Ye, H. (2023). Bridge frequency identification based on relative displacement of axle and contact point using tire pressure monitoring. *Mechanical Systems and Signal Processing*, *183*, Article 109613. https://doi.org/10.1016/j.ymssp.2022.109613

Liu, J. X., Chen, S. H., Bergés, M., Bielak, J., Garrett, J. H., Kovačević, J., & Noh, H. Y. (2020). Diagnosis algorithms for indirect structural health monitoring of a bridge model via dimensionality reduction. *Mechanical Systems and Signal Processing*, *136*, Article 106454. https://doi.org/10.1016/j.ymssp.2019.106454

Malekzadeh, M., Gül, M., Kwon, I. B., & Catbas, N. (2014). An integrated approach for structural health monitoring using an in-house built fiber optic system and non-parametric data analysis. *Smart Structures and Systems*, *14*(5), 917–942. https://doi.org/10.12989/sss.2014.14.5.917

McGetrick, P. J., González, A., & OBrien, E. J. (2009). Theoretical investigation of the use of a moving vehicle to identify bridge dynamic parameters. *Insight: Non-Destructive Testing and Condition Monitoring, 51*(8), 433–438. https://dx.doi.org/10.1784/insi.2009.51.8.433

Nayek, R., & Narasimhan, S. (2020). Extraction of contact-point response in indirect bridge health monitoring using an input estimation approach. *Journal of Civil Structural Health Monitoring, 10*(5), 815–831. https://doi.org/10.1007/s13349-020-00418-z

OBrien, E. J., & Keenahan, J. (2015). Drive-by damage detection in bridges using the apparent profile. *Structural Control and Health Monitoring, 22*(5), 813–825. https://doi.org/10.1002/stc.1721

Quirke, P., Bowe, C., OBrien, E. J., Cantero, D., Antolin, P., & Goicolea, J. M. (2017). Railway bridge damage detection using vehicle-based inertial measurements and apparent profile. *Engineering Structures, 153*, 421–442. https://dx.doi.org/10.1016/j.engstruct.2017.10.023

Railway Accident Investigation Unit. (2010). *Malahide Viaduct Collapse on the Dublin to Belfast Line, on the 21st August 2009* (Report No. 2010 – R004).

Rytter, A. (1993). *Vibrational based inspection of civil engineering structures* [Doctoral dissertation, Aalborg University]. Aalborg University Publications. https://vbn.aau.dk/ws/portalfiles/portal/549415878/Vibrational_Based_Inspection_of_Civil_Engineering_Structures

Sayers, M. W., & Karamihas, S. M. (1996). *Interpretation of road roughness profile data* (Report No. FHWA-RD-96-101). The University of Michigan Transportation Research Institute.

Sinha, J. K., Friswell, M. I., & Edwards, S. (2002). Simplified models for the location of cracks in beam structures using measured vibration data. *Journal of Sound and Vibration, 251*(1), 13–38. https://doi.org/10.1006/jsvi.2001.3978

Siringoringo, D. M., & Fujino, Y. (2012). Estimating bridge fundamental frequency from vibration response of instrumented passing vehicle: Analytical and experimental study. *Advances in Structural Engineering, 15*(3), 417–433. https://doi.org/10.1260/1369-4332.15.3.417

Soman, R., Kyriakides, M., Onoufriou, T., & Ostachowicz, W. (2018). Numerical evaluation of multi-metric data fusion based structural health monitoring of long span bridge structures. *Structure and Infrastructure Engineering, 14*(6), 673–684. https://doi.org/10.1080/15732479.2017.1350984

Tan, C. J., Elhattab, A., & Uddin, N. (2017). "Drive-by'' bridge frequency-based monitoring utilizing wavelet transform. *Journal of Civil Structural Health Monitoring, 7*(5), 615–625. https://doi.org/10.1007/s13349-017-0246-3

Yang, Y. B., Li, Y. C., & Chang, K. C. (2012). Using two connected vehicles to measure the frequencies of bridges with rough surface: A theoretical study. *Acta Mechanica, 223*(8), 1851–1861. https://doi.org/10.1007/s00707-012-0671-7

Yang, Y. B., & Lin, C. W. (2005). Vehicle-bridge interaction dynamics and potential applications. *Journal of Sound and Vibration, 284*(1–2), 205–226. https://doi.org/10.1016/j.jsv.2004.06.032

Yang, Y. B., Lin, C. W., & Yau, J. D. (2004). Extracting bridge frequencies from the dynamic response of a passing vehicle. *Journal of Sound and Vibration, 272*(3–5), 471–493. https://doi.org/10.1016/S0022-460X(03)00378-X

Yang, Y. B., Zhang, B., Qian, Y., & Wu, Y. T. (2018). Contact-point response for modal identification of bridges by a moving test vehicle. *International Journal of Structural Stability and Dynamics, 18*(5), Article 1850073. https://doi.org/10.1142/S0219455418500736

Yeh, K. C., & Kwan, K. C. (1978). A comparison of numerical integrating algorithms by trapezoidal, Lagrange, and spline approximation. *Journal of Pharmacokinetics and Biopharmaceutics, 6*(1), 79–98. https://doi.org/10.1007/BF01066064

Yin, X. F., Liu, Y., Deng, L., & Kong, X. (2017). Dynamic behavior of damaged bridge with multi-cracks under moving vehicular loads. *International Journal of Structural Stability and Dynamics, 17*(2), Article 1750019. https://doi.org/10.1142/S0219455417500195

Zhan, Y., Au, F. T. K., & Yang, D. (2020). Extraction of bridge information based on the double-pass double-vehicle technique. *Smart Structures and Systems, 25*(6), 679–691. https://doi.org/10.12989/sss.2020.25.6.679

Zhan, Y., Au, F. T. K., & Zhang, J. (2021). Bridge identification and damage detection using contact point response difference of moving vehicle. *Structural Control Health Monitoring, 28*(12), Article 2837. https://doi.org/10.1002/stc.2837